

Turbulent/nonturbulent interfaces in high-resolution direct numerical simulation of temporally evolving compressible turbulent boundary layers

Xinxian Zhang, Tomoaki Watanabe,* and Koji Nagata

Department of Aerospace Engineering, Nagoya University, Furo-cho, Chikusa-ku, Nagoya 464-8603, Japan



(Received 4 December 2017; published 18 September 2018)

Turbulent/nonturbulent interfaces (TNTIs) are studied in the direct numerical simulation of temporally evolving turbulent boundary layers at Mach numbers 0.8 and 1.6 with Reynolds number based on the momentum thickness of about 2200. The computational grid size determined based solely on the wall unit results in insufficient resolutions near the TNTI even though it yields the well-known profiles of global statistics such as mean velocity and rms velocity fluctuations. The insufficient resolution near the TNTI layer causes the spiky patterns of the enstrophy isosurface used for detecting the outer edge of the TNTI layer and the thicker TNTI layer thickness. With the higher-resolution direct numerical simulation, where the resolution is determined based on both the wall unit and the smallest length scale of turbulence underneath the TNTI layer, we investigate the structures of the TNTI layer and the entrainment process in the compressible turbulent boundary layers. The mean vorticity profile and enstrophy evolutions near the TNTI layer show that the structure of the TNTI layer is similar to incompressible free shear flows: The thickness of the layer is about 15 times the Kolmogorov scale η_l in turbulence near the TNTI layer; the turbulent sublayer (TSL) and viscous superlayer (VSL) are found based on the analysis of enstrophy transport equation, where the thicknesses of the TSL and VSL are $11\eta_l$ – $12\eta_l$ and $4\eta_l$, respectively. The entrainment process across the TNTI layer is also studied based on the propagation velocity of the enstrophy isosurface and the mass transport equation in the local coordinate moving with the TNTI. The entrainment mechanism across the TNTI layer in compressible turbulent boundary layers is very similar to incompressible free shear flows until Mach number 1.6, where the mass transport within the TNTI layer is well predicted by an entrainment model based on a single vortex originally developed for incompressible flows. Furthermore, the mass entrainment rate per unit horizontal area of the temporally evolving turbulent boundary layers is consistent with the theoretical prediction for spatially evolving compressible turbulent boundary layers for both Mach numbers.

DOI: [10.1103/PhysRevFluids.3.094605](https://doi.org/10.1103/PhysRevFluids.3.094605)

I. INTRODUCTION

Turbulent boundary layers (TBLs) play an important role in many engineering applications and geophysical flows. For example, the development and separation of boundary layers can significantly influence the body force and instability of airfoils or vehicles. Therefore, a large number of studies have been devoted to understanding TBLs from various points of view. In these engineering applications, the TBL often develops in a freestream at transonic or supersonic velocity, where compressibility is significant in the flow evolution [1].

*watanabe.tomoaki@c.nagoya-u.jp

Prandtl [2] pointed out the existence of a sharp interface between turbulent and nonturbulent flows, which is called the turbulent/nonturbulent interface (TNTI). After decades, the existence of the TNTI was examined in a free shear layer by Corrsin and Kistler [3]. Recently, with the increase of supercomputer resources and the use of laser-based measurement techniques, many studies have been focusing on this interface [4]. The TNTI appears in many canonical flows such as jets, wakes, and boundary layers. The flow properties near the TNTI in these flows have been investigated with the conditional statistics computed as a function of the distance from the TNTI [5]. These recent studies have revealed that the TNTI is a thin layer with finite thickness. The TNTI layer consists of two (sub)layers with different dynamical characteristics. The outer part is called the viscous superlayer (VSL), where viscous effects dominate vorticity evolution, while the region between the VSL and turbulent core region is called the turbulent sublayer (TSL) [4], where the inviscid effects, such as vortex stretching, become important.

The turbulent and nonturbulent flow regions are separated by this TNTI layer, where flow properties such as enstrophy, kinetic energy dissipation, and scalar concentration sharply change so that they are adjusted between the turbulent and nonturbulent flows [6]. This layer is also important for the exchanges of substance, energy, and heat between turbulent and nonturbulent flows and is also related to the spatial development of turbulence [7]. These phenomena are associated with the turbulent entrainment process [4], in which the fluid in the nonturbulent region is transported to the turbulent region. The entrainment processes caused by large-scale and small-scale eddies are often referred to as engulfment and nibbling, respectively. The nibbling-type entrainment is caused by the viscous diffusion of vorticity in the proximity of the TNTI layer, while the engulfment is described with the nonturbulent flow that is drawn into the turbulent region by large-scale eddies before acquiring vorticity. The dominant mechanism for the entrainment process has been argued for many years. Recent studies have suggested that the nibbling process is responsible for the entrainment mechanism and large-scale features of turbulence impose the total entrainment rate [7–9]. The geometry of the TNTI is an important issue for understanding the entrainment process: The large pocket structure on the TNTI interface can indraft the nonturbulent fluids into the turbulent region before acquiring vorticity (engulfment) if the TNTI interface is intensely folded [10]. It is doubtless that the complex geometry of the interface is highly related to the total entrainment rate. Therefore, it may need more information for the relation between nibbling and engulfment as mentioned by Borrell and Jiménez [11]. The relative importance of the engulfment can be flow dependent because large-scale motions depend on flow types. The turbulent flow under the TNTI layer contains eddies with a wide range of scales, and all length scales can affect the properties and geometry of the TNTI layer. Therefore, motions from the smallest to the largest scales need to be captured in measurement or simulations. Especially in the simulations, all scales should be resolved; insufficient resolution can directly affect computational results. Recently, the TNTI in incompressible TBLs have been studied in experiments [12–15] and direct numerical simulations [11, 15–17]. These recent studies have revealed the influence of large-scale structures on the geometry of the TNTI in the boundary layer [15, 18], which can make differences in the entrainment process between the TBLs and free shear flows.

Understanding the characteristics of the TNTI is greatly important in modeling and predicting the spatial development of turbulence as well as the flow control based on the turbulent structures near the TNTI. Even though the TNTI has been extensively studied in recent studies on free shear flows, the conceptual gaps still exist in the modeling issue [19]. Although some similar characteristics of the TNTI are also found in the TBL [17], the TNTI in TBLs is still lacking information compared to the free shear flows. So far, most studies on the TNTI have been done in incompressible flows, although a high-speed regime, where compressibility plays an important role, is of great importance in realistic full-scale applications. Compressibility effects on the TNTI have been studied in compressible mixing layers [20–23]. However, the TNTI in compressible turbulence is still less understood compared with the one in incompressible flows.

In this study, direct numerical simulation (DNS) is performed for temporally developing subsonic and supersonic TBLs in order to investigate the characteristics of the TNTI in the compressible

TBLs. We pay particular attention to the resolution near the TNTI, which is usually ignored in numerical simulations of boundary layers in the existing literature. We assess the influence of the spatial resolution near the TNTI on the analysis of the TNTI. This paper is organized as follows. The details of DNS are presented in Sec. II. In Sec. III, the classical statistics of the boundary layers are compared with previous studies. Section IV discusses the effects of resolution followed by the statistical analysis of compressible TBLs. Section V summarizes the work.

II. DIRECT NUMERICAL SIMULATION OF TEMPORALLY EVOLVING COMPRESSIBLE BOUNDARY LAYERS

A. Temporally evolving compressible boundary layers

The DNS is performed for temporally evolving compressible TBLs. The temporal simulations are useful because the boundary layer grows so slowly in the streamwise direction that the turbulence can be treated approximately as homogeneous in this direction. In recent numerical studies, temporal simulations were successfully applied to TBLs [24,25], where the statistics compare well with experimental results.

The governing equations are the three-dimensional Navier-Stokes equations for compressible flows. The conservation equations of mass, momentum, energy, and passive scalar ϕ are expressed as [26]

$$\frac{\partial \rho}{\partial t} + \frac{\partial \rho u_j}{\partial x_j} = 0, \quad (1)$$

$$\frac{\partial \rho u_i}{\partial t} + \frac{\partial \rho u_i u_j}{\partial x_j} = -\frac{\partial P}{\partial x_i} + \frac{\partial \tau_{ij}}{\partial x_j}, \quad (2)$$

$$\frac{\partial \rho T}{\partial t} + \frac{\partial \rho T u_j}{\partial x_j} = -(\gamma - 1)P \frac{\partial u_j}{\partial x_j} + \gamma \frac{\partial}{\partial x_j} \left(k \frac{\partial T}{\partial x_j} \right) + (\gamma - 1)\tau_{ij} \frac{\partial u_i}{\partial x_j}, \quad (3)$$

$$\frac{\partial \rho \phi}{\partial t} + \frac{\partial \rho u_j \phi}{\partial x_j} = \frac{\partial}{\partial x_j} \left(\rho D_m \frac{\partial \phi}{\partial x_j} \right), \quad (4)$$

with the equation of state for the perfect gas $P = \rho RT$, where the viscous stress tensor τ_{ij} is represented by

$$\tau_{ij} = \mu \left(\frac{\partial u_i}{\partial x_j} + \frac{\partial u_j}{\partial x_i} - \frac{2}{3} \delta_{ij} \frac{\partial u_k}{\partial x_k} \right). \quad (5)$$

Here ρ is the density, u_i is the velocity, P is the pressure, T is the temperature, μ is the viscosity, k is the thermal conductivity, D_m is the molecular diffusivity for the passive scalar ϕ , and $\gamma = C_p/C_v = 1.4$ and $R = C_p - C_v = 287$ [J/(kg K)] are the ratios between specific heats and the gas constant, respectively. The temperature-dependent viscosity μ is provided by Sutherland's law

$$\mu = \mu_s \left(\frac{T}{T_s} \right)^{3/2} \frac{T_s + S}{T + S}, \quad (6)$$

where $\mu_s = 1.742 \times 10^{-5}$ Pa s, $T_s = 273$ K, and $S = 110.4$ K. We assume that the Prandtl number $\text{Pr} = \mu C_p/k = 0.71$ and the Schmidt number $\text{Sc} = \mu/\rho D_m = 1$.

A three-dimensional computational domain with a size of $(L_x \times L_y \times L_z)$ is considered, where the wall is at the bottom of the computational domain. The origin of the coordinate system is located at the center of the wall, while the streamwise, wall-normal, and spanwise directions are represented by x , y , and z , respectively. The initial conditions used in the present DNSs are similar to the ones introduced in Ref. [27]. The initial velocity profile approximates the velocity induced by a trip wire with a diameter D installed on the wall, which is moving in the x direction at a constant speed U_w [28] (the subscript w represents a quantity on the wall). We consider the fluid at pressure $P_a = 101.3$ kPa, temperature $T_a = 300$ K, and density $\rho_a = P_a/RT_a$, where the subscript a refers

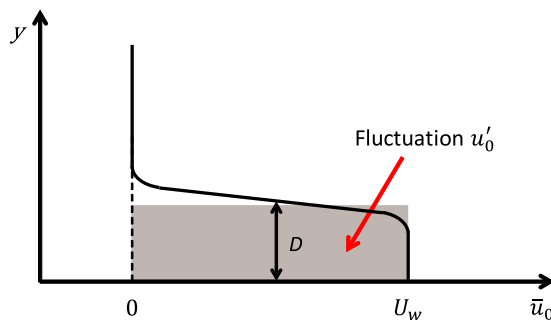


FIG. 1. Initial streamwise velocity profile used in DNS of temporally developing boundary layers.

to the atmospheric parameters. The trip wire is often used in wind tunnel experiments to promote the transition from the laminar to the turbulent boundary layer [29]. The initial mean streamwise velocity profile is given by a hyperbolic tangent profile that is equal to the wall velocity U_w at $y = 0$ and decreases toward 0 as y increases as shown in Fig. 1, where the overbar denotes the averaged value calculated with the spatial averaging procedure applied in the streamwise and spanwise (x and z) directions and the subscript 0 refers to an initial value. The initial velocity field consists of a mean velocity and fluctuating components. Specifically, the initial streamwise velocity u_0 can be written as [27]

$$u_0 = \bar{u}_0(y) + u'_0(x, y, z), \quad (7)$$

$$\bar{u}_0(y) = \frac{U_w}{2} + \frac{U_w}{2} \tanh \left[\frac{D}{2\theta_{SL}} \left(1 - \frac{y}{D} \right) \right], \quad (8)$$

where u'_0 is the velocity fluctuation and $\theta_{SL} = 0.1D$ is the initial shear layer thickness. In order to trigger a turbulent transition, the velocity fluctuations with the root-mean-square (rms) value $0.05U_w$ are added to all velocity components in the near-wall region of $y < D$ as shown in Fig. 1. The velocity fluctuations are generated by a diffusion process that converts the random noise into fluctuations which possess a prescribed length scale [30]. Mean velocities in the spanwise and wall-normal directions are zero at the initial state. Initial profiles of temperature and pressure are uniform, where $T_0 = T_a$ and $P_0 = P_a$. The initial condition of ϕ is given by the profile

$$\phi = \frac{\phi_w}{2} + \frac{\phi_w}{2} \tanh \left[\frac{D}{2\theta_{SL}} \left(1 - \frac{y}{D} \right) \right]. \quad (9)$$

The Reynolds number based on the trip wire diameter D is $Re_D \equiv \rho_a U_w D / \mu_0 = 2000$, which is higher than the critical value for the turbulent transition ($Re_D = 500$) in temporally evolving incompressible boundary layers [27]. The DNS is performed with two different Mach numbers $M = 0.8$ and 1.6 defined as $M = U_w / c_0$ (c_0 is the speed of sound at the initial state), which correspond to subsonic and supersonic boundary layers, respectively. We will discuss the TNTI in the TBLs at the time when the Reynolds number based on the momentum thickness, $Re_\theta = \rho_\infty U_w \theta / \mu_\infty$, reaches about 2200, where the subscript ∞ refers to the properties in the freestream far from the boundary layer and $\theta = \int_0^\infty (\bar{\rho} u / \rho_\infty U_w) [1 - (\bar{u} / U_w)] dy$ is the momentum thickness.

For temporally developing TBLs, the periodic boundary conditions are applied in the streamwise (x) and spanwise (z) directions. In the wall-normal direction (y), the no-slip adiabatic condition with the passive scalar $\phi = 1$ is applied on the wall ($y = 0$), while at the top of the computational domain ($y = L_y$), the nonreflective outflow boundary conditions of three-dimensional (3D) Navier-Stokes characteristics boundary conditions (NSCBCs) are used with a sponge layer [31] for the fluid field as well as passive scalar field, to prevent the spurious wave reflections on the boundary. The 3D NSCBC used in present DNS was proposed by Lodato *et al.* [31] as a modified version of the

original NSCBC. In the 3D NSCBC, convection and the pressure gradient on boundary planes are considered. The sponge layer [32] is located in the region of $L_y - 10D < y < L_y$, where the fluctuations induced by pressure waves are damped by a low-pass filter before the waves reach the top boundary. The mean flow variables in the sponge zone are also adjusted so that they match the classical laws observed in TBLs [32]. The sponge layer in the present DNS is formed by combining the coarse grid stretched in the boundary normal direction and Laplacian low-pass filtering.

B. Numerical methods used in DNS code

The present DNS code is based on the fully explicit numerical schemes proposed by Wang *et al.* [33]. For the spatial discretization, the explicit eighth-order central difference scheme is used for the interior nodes, while the nodes near the computational boundaries are treated with internal-biased lower-order finite-difference schemes for stability unless the periodic boundary conditions are applied [33]. The convective terms in the governing equations are calculated in the cubic skew symmetric form [34], which can reduce aliasing error caused by the finite-difference schemes [35]. The time integration of the governing equations is also based on the fully explicit schemes following [33]. The Euler and viscous terms are handled by different numerical schemes, where the explicit five-stage fourth-order Runge-Kutta method [36] is used for the Euler terms while the explicit first-order Euler scheme is used for the viscous terms, which arise from viscous effects, thermal conductive diffusion, and molecular diffusion of ϕ . Finally, to remove the spurious fluctuations induced by the finite-difference schemes, a tenth-order low-pass filter [37] is applied on the whole computational domain at each time step. The time-step interval is determined by the Courant-Friedrichs-Lewy (CFL) condition and a CFL condition equal to 0.8 is used in this study. These numerical schemes were used in the DNS of a subsonic round jet [38] and a diffusion jet flame [33] and are proven to be able to accurately simulate compressible turbulence.

C. Computational parameters in DNS

The computational domain (L_x, L_y, L_z) should be large enough to contain a large number of large-scale flow structures to prevent the periodic boundary conditions from affecting the flow development. In the present DNS, L_x, L_y , and L_z are determined based on the boundary layer thickness δ in the fully developed region, where δ is defined as the vertical location y at which the streamwise mean velocity \bar{u} reaches 1% of the wall velocity U_w [39]. The wall-parallel domain size is set so that $L_x \approx 6\delta$ in the streamwise direction and $L_z \approx 3\delta$ in the spanwise direction. For the wall-normal direction, we use $L_y \approx 3\delta + 10D$ (here $10D$ is the thickness of the sponge layer). Here the values of δ are taken from the instance at which the detailed analysis is performed in this study. The size of the computational domain in relation to δ is similar to the one by Kozul *et al.* [27].

The Cartesian mesh is used in this study, where the grid spacing is uniform in the x and z directions, while the wall-normal grid spacing obeys a half-tanh mapping, which gives a finer grid near the wall and a coarser grid away from the wall by stretching the grid as y increases. To study the TNTI, the resolution near the TNTI should be carefully examined, where the DNS must resolve the smallest scale of turbulence that appears underneath the TNTI, i.e., the Kolmogorov scale $\eta = (\bar{v}^3/\bar{\varepsilon})^{1/4}$ in the turbulent region. [Here $\varepsilon = \tau_{ij}S_{ij}$ is the kinetic energy dissipation rate, $S_{ij} = (\partial u_i/\partial x_j + \partial u_j/\partial x_i)/2$ is the rate of strain tensor, and $\nu = \mu/\rho$ is the kinematic viscosity.] To investigate the effects of the resolution near the TNTI, we perform the DNS with two different meshes for each value of the Mach number as summarized in Table I. The DNS with resolution similar to the DNS of conventional wall turbulence is referred to as group C (cases C001 and C002 for $M = 0.8$ and 1.6 , respectively), where the resolution is determined based on the structures of the near-wall region [25,40]. The spatial resolution in group C is determined based on the smallest viscous length scale $\delta_{v,\min}$ during the whole simulation, where the viscous length scale is defined as $\delta_v = \bar{v}_w/u_\tau$ with the friction velocity $u_\tau = \sqrt{\tau_w/\bar{\rho}_w}$ (the viscous velocity scale) and the wall shear stress $\tau_w \equiv \bar{\mu}_w(-d\bar{u}/dy)_w$. Following previous studies, we ensure that the mesh sizes satisfy

TABLE I. Computational parameters and Reynolds numbers obtained in fully developed turbulent states of boundary layers for which detail analysis is performed in this study.

Case	M	Re_θ	Re_τ	L_x/δ	L_y/δ	L_z/δ	Δx^+	Δy_w^+	Δz^+	N_x, N_y, N_z
F001	0.8	2206	639	6.30	5.37	3.15	4.6	0.188	4.6	972, 738, 486
F002	1.6	2174	524	7.23	5.92	3.62	4.9	0.180	4.6	972, 772, 512
C001	0.8	2315	707	5.74	4.89	2.87	9.5	0.188	4.8	486, 628, 486
C002	1.6	2403	554	6.53	5.34	3.27	8.4	0.180	4.7	576, 648, 512

$\Delta x^+ < 9.7$ and $\Delta z^+ < 4.8$ for the streamwise and spanwise directions, respectively [41], and $\Delta y_w^+ < 0.2$ (the quantities with superscript + are normalized by the viscous scale) for wall-normal direction. The simulations in the group F (cases F001 and F002 for $M = 0.8$ and 1.6 , respectively) are performed with finer meshes than the group C. The number of grid points in the group F is determined not only based on the length of the near-wall region $\delta_{v, \min}$ but also based on the Kolmogorov scale η_c in the turbulent core region away from the wall ($y = 0.5\delta$), where the subscript c represents a value in the turbulent core region. The difference in the resolution between groups C and F is discussed in relation to the TNTI in Sec. IV. Thereby, the number of the grid points (N_x , N_y , and N_z) is determined from the required resolutions and computational domain size. Finally, the parameters of the computational domain, grid, and computational parameters are shown in Table I, which also includes Re_θ and friction Reynolds number $Re_\tau = \bar{\rho}_w u_\tau \delta / \bar{\mu}_w$ in the fully developed turbulent states of the boundary layers for which detail analysis is performed in this study.

III. COMPUTATIONAL RESULTS AND VALIDATION

The development of the TBLs is well examined by the passive scalar ϕ , which is equal to ϕ_w on the wall and 0 in the freestream. Figure 2 shows the two-dimensional snapshots of ϕ at different times throughout the simulation for case F001 ($M = 0.8$), which offer a view of the boundary layer development process in the temporal DNS. We can see that the boundary layer develops from a laminar flow in Fig. 2(a) to a turbulent flow in Figs. 2(b) and 2(c) and reaches the fully developed state as in Fig. 2(d). The passive scalar ϕ can be used as a marker of the turbulent region [42], where $\phi/\phi_w > 0$. We can also see that the nonturbulent fluids with $\phi/\phi_w = 0$ coexist with the turbulent fluids in the intermittent region for the TBL.

In order to compare the skin friction coefficient $C_f = 2\tau_w/\bar{\rho}_w U_w^2$ at different Mach numbers M , it is necessary to transform the compressible values to incompressible values [43], where the incompressible values are denoted by the subscript i :

$$C_{f,i} = F_c C_f, \quad Re_{\theta,i} = \frac{\mu_\infty}{\bar{\mu}_w} Re_\theta, \quad (10)$$

$$F_c = \frac{\bar{T}_w/T_\infty - 1}{\arcsin^2 \alpha_2}, \quad \alpha_2 = \frac{\bar{T}_w/T_\infty - 1}{\sqrt{\bar{T}_w/T_\infty (\bar{T}_w/T_\infty - 1)}}. \quad (11)$$

The variation of the transformed skin friction $C_{f,i}$ versus $Re_{\theta,i}$ for the present DNS is compared in Fig. 3(a) with a widely used friction law of TBLs [44]: $C_{f,i} = 0.024 Re_{\theta,i}^{-1/4}$. It is important to note that Re_θ increases with time t because the boundary layer is also developed with time. We can see that the skin frictions obtained from the present DNS are in better agreement with the friction law for higher Re_θ . This implies that the boundary layers undergo the transition from the laminar state to the fully developed turbulent state. The temporal variation in $(C_{f,i}, Re_{\theta,i})$ in the present DNS also agrees well with previous DNSs of temporally developing boundary layers [27].

The mean profiles of the Van Driest transformed streamwise velocity [45] are plotted in Fig. 3(b) for two Mach numbers, where we use the snapshot at which $Re_\theta \approx 2200$ as summarized in Table I.

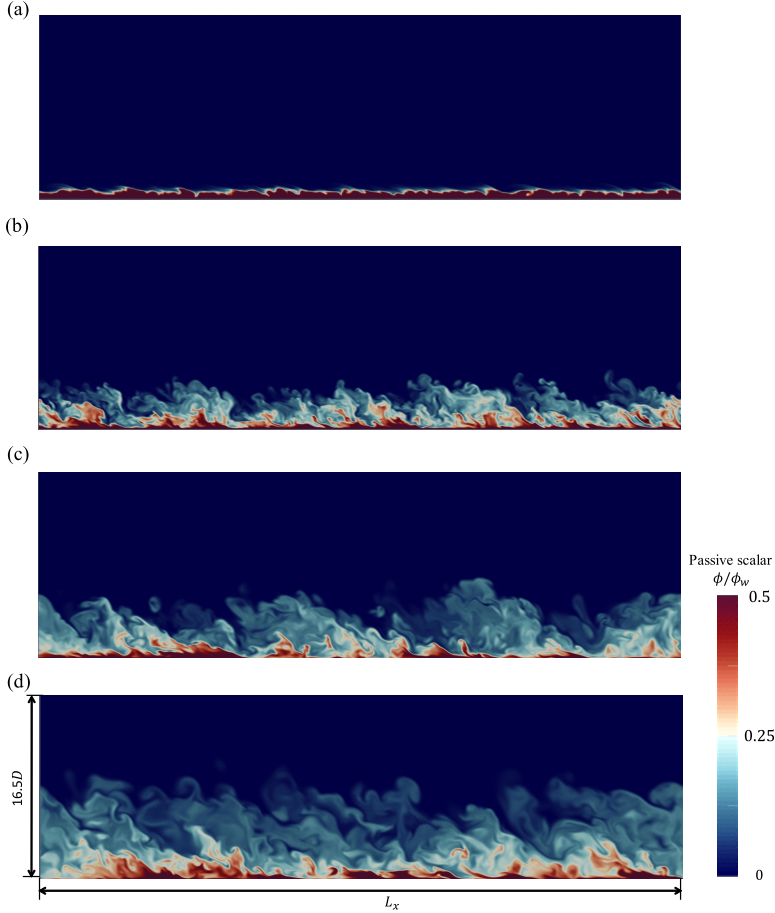


FIG. 2. Visualization of the temporally developing boundary layer with passive scalar ϕ for case F001. The wall is moving in the x direction (from left to right). The parameters are (a) $t/t_r = 8.2$, $Re_\theta = 278$, and $Re_\tau = 6$; (b) $t/t_r = 54.1$, $Re_\theta = 1336$, and $Re_\tau = 327$; (c) $t/t_r = 136.5$, $Re_\theta = 1764$, and $Re_\tau = 495$; and (d) $t/t_r = 260.1$, $Re_\theta = 2152$, and $Re_\tau = 622$.

The definitions of the Van Driest transformed [45] streamwise velocity u_{VD} and normalized wall-normal distance y^+ [39] are given by

$$u_{VD}(y) = \int_0^{u^+} \sqrt{\frac{\bar{\rho}(y)}{\bar{\rho}_w}} du^+, \quad u^+(y) = [U_w - \bar{u}(y)]/u_\tau, \quad (12)$$

$$y^+ = y/\delta_v. \quad (13)$$

The green dotted line indicates $u_{VD} = y^+$, which should hold for the viscous sublayer, and the red dashed line is the log-law represented as $u_{VD} = (1/k)\ln y^+ + A$ [39]. In the viscous sublayer ($y^+ < 5$), the Reynolds shear stress is negligible compared to the viscous stress and the DNS data agree well with the green dotted line; in the log-law region, where the viscous effects on the mean velocity \bar{u} are ignored, the present DNS results are in good agreement with the log-law with the constants $k = 0.41$ and $A = 5.1$. The profiles of $y^+ du_{VD}/dy^+$ are shown in Fig. 4 to check values of k , where the log-law region satisfies $y^+ du_{VD}/dy^+ = 1/k$. The curves in the figures

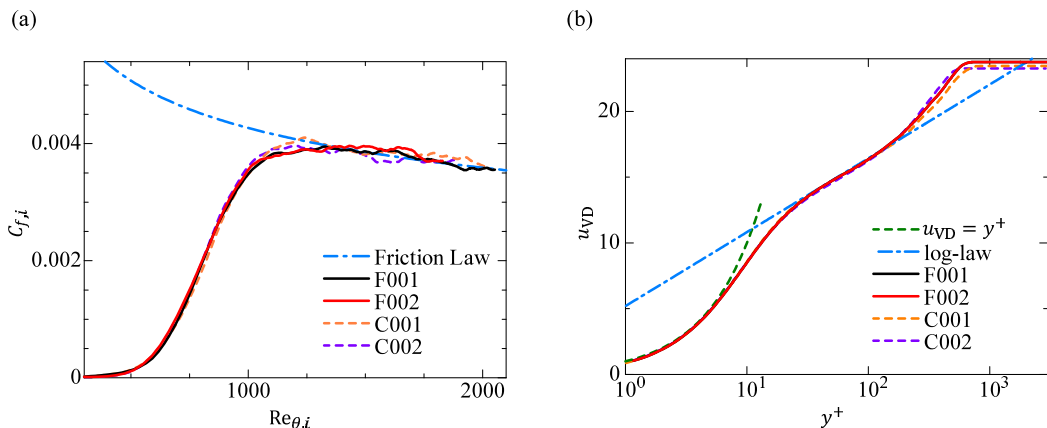


FIG. 3. (a) Variations of the skin friction coefficient $C_{f,i}$ versus Reynolds number $Re_{\theta,i}$. (b) Van Driest transformed streamwise velocity profiles.

represent different time steps in the fully developed TBLs at $Re_{\theta} \approx 2200$. There is a region where $y^+ du_{VD}/dy^+$ is close to $1/k$ with $k = 0.41$, although $y^+ du_{VD}/dy^+$ does not follow the horizontal line. This is because it is difficult to obtain converged statistics in temporal simulations [27]. The moderate Reynolds number in the present DNS also causes difficulty in observing a clear log-law region. We can see that 0.41 is close to the average of k in the possible log-law region in these figures. It should be noted that $k = 0.40$ – 0.41 was widely used in previous studies of compressible boundary layers [46–48]. Even in these previous studies, the exact location of the beginning of the log-law region was not thoroughly discussed for compressible TBLs [49].

The second-order statistics are compared with experimental data [50] and other DNS data [51] of incompressible TBLs in Fig. 5. As described in Morkovin’s hypothesis [52], the compressibility mainly affects the density and thermodynamic properties across the boundary layer rather than the turbulence timescale and length scale for moderate Mach numbers ($M < 5$) [1]. Therefore, DNS of compressible boundary layers is usually validated in comparison with incompressible flows for a similar Re_{θ} . The following transformation of second-order statistics of velocity in the compressible

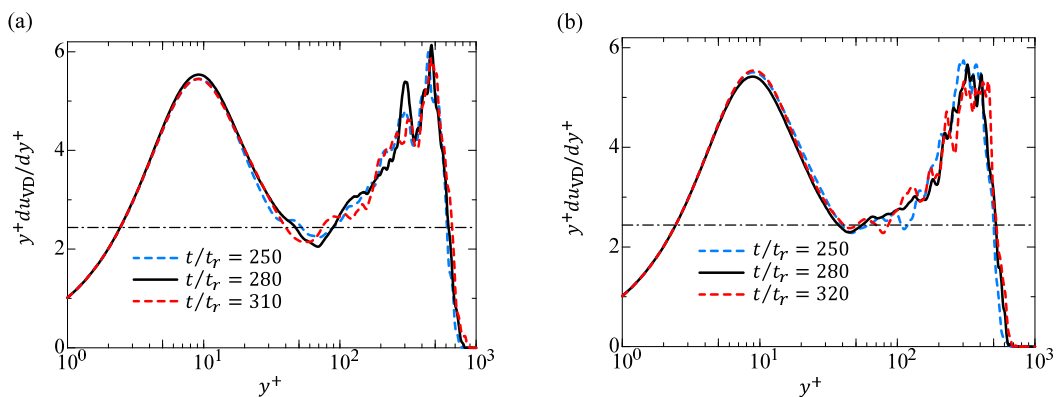


FIG. 4. Compensated mean velocity profiles $y^+ du_{VD}/dy^+$ in (a) case F001 and (b) case F002. The black dash-dotted line denotes the reference $y^+ du_{VD}/dy^+ = 1/k$ with $k = 0.41$.

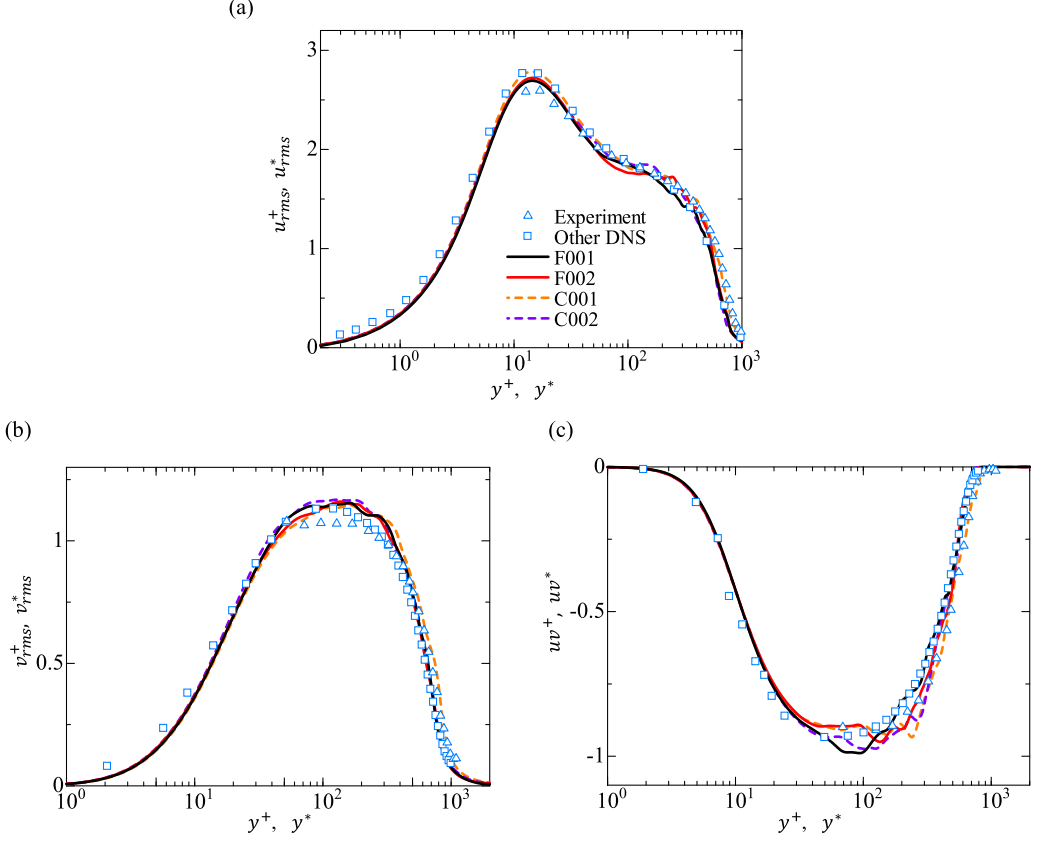


FIG. 5. Second-order statistics: (a) rms streamwise velocity fluctuation, (b) rms wall-normal velocity fluctuation, and (c) Reynolds stress. The present DNS results are compared with incompressible TBLs studied in experiments at $Re_\theta = 2266$ [50] and in DNS at $Re_\theta = 1986$ [51].

boundary layers is required for the comparison [53]

$$u_i u_j^* = \frac{\widetilde{u_i'' u_j''} \bar{\rho}(y)}{u_\tau^2 \bar{\rho}_w}, \quad u_i'' = u_i - \widetilde{u}_i, \quad u_{i,rms}^* = \sqrt{u_i u_i^*}, \quad (14)$$

$$y^* = y/\delta_v^*, \quad \delta_v^*(y) = \bar{v}(y)/u_\tau \sqrt{\bar{\rho}_w/\bar{\rho}(y)}, \quad (15)$$

where \widetilde{f} is a density-weighted average (Favre average) $\widetilde{f} = \overline{\rho f}/\bar{\rho}$. The statistics from incompressible TBLs are nondimensionalized by the viscous scales as follows:

$$u_i u_j^+ = \frac{\overline{u_i' u_j'}}{u_\tau^2}, \quad u_i' = u_i - \bar{u}_i, \quad u_{i,rms}^+ = \sqrt{u_i u_i^+}, \quad (16)$$

$$y^+ = y/\delta_v. \quad (17)$$

As shown in Fig. 5, we can find excellent agreement for the rms streamwise velocity fluctuation in Fig. 5(a), the rms wall-normal velocity fluctuation in Fig. 5(b), and the Reynolds stress in Fig. 5(c) for a comparable value of Re_θ . There are scatters in the statistics in the present DNS in the outer region, which is explained by the limited number of samples in temporal simulations as pointed out in Ref. [27]. By comparisons of first- and second-order statistics, the results show that the temporal DNS performed here accurately replicates the compressible TBLs for both computational meshes

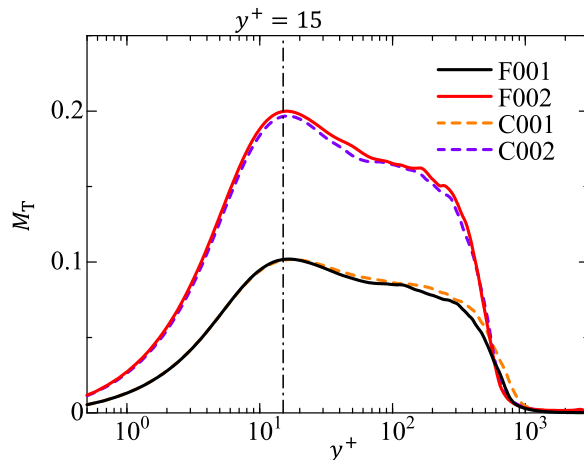


FIG. 6. Vertical profiles of the turbulent Mach number.

of groups F and C. Note that the skin friction, mean velocity, and rms velocity fluctuations in the compressible boundary layers presented above are consistent with those in incompressible boundary layers because of the Van Driest transformation.

The turbulent Mach number M_T is shown in Fig. 6, where M_T implying the significance of compressibility effects is defined as

$$M_T = \frac{(\overline{u'_i u'_i})^{1/2}}{c}, \quad (18)$$

where $c = \sqrt{\gamma RT}$ is the local speed of sound. As shown in Fig. 6, the largest M_T is located in the buffer layer about $y^+ = 15$, which refers to the location where the peak turbulence production occurs. Since M_T is less than 0.3 throughout the boundary layers for $M = 0.8$ and 1.6, the compressibility is not strong enough to significantly change turbulence structures and the TBL develops in the absence of shock waves [1].

IV. TURBULENT/NONTURBULENT INTERFACE AND ENTRAINMENT PROCESS

A. Detection of the turbulent/nonturbulent interface

As in previous studies on the TNTI layer [4,54], an isosurface of vorticity magnitude $\omega = \omega_{th}$ is used to detect the outer edge of the TNTI, which is called the irrotational boundary [54]. Since the location of the isosurface of vorticity magnitude changes with the threshold ω_{th} , it is important to choose a reasonable value of ω_{th} . In this study, the threshold ω_{th} is determined based on the volume fraction of the turbulent region V_T computed as a function of ω_{th} ; this approach was widely used for detecting turbulent and nonturbulent fluids in previous studies [4,11,54] including compressible flows [20] and is also related to the method to obtain the threshold based on the probability density function of vorticity magnitude [17]. These two methods have been shown to yield a similar value of threshold [17]. The latter method has been used also in the detection of a scalar interface in experiments [55]. A fluid with $\omega > \omega_{th}$ is referred to as a turbulent fluid, while a nonturbulent fluid has $\omega < \omega_{th}$. The normalized threshold applied for the vorticity magnitude in the TBL is

$$\omega_{th}^* = \frac{\omega_{th}}{(\delta^+)^{-1/2} u_\tau^2 / \bar{v}_w}, \quad (19)$$

where δ^+ is the boundary layer thickness normalized by the viscous length scale, which is also equal to Re_τ . This scaling is linked to the TNTI interface because the TNTI layer appears around the

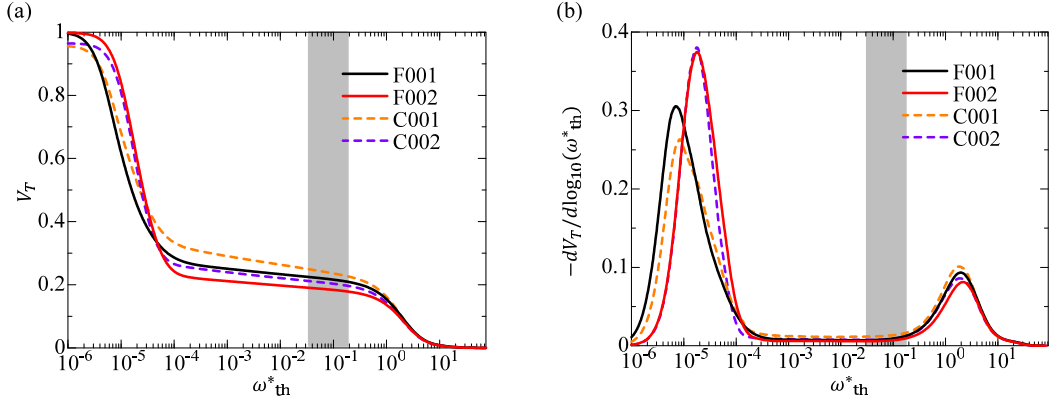


FIG. 7. (a) Volume fractions of the turbulent region V_T plotted against the threshold ω_{th}^* used for detecting turbulent fluids. (b) First derivative of the volume fraction $dV_T/d \log_{10}(\omega_{th}^*)$. The several values of vorticity magnitude in the range of the gray shadow will be used to examine the robustness of irrotational boundary detection in the next section.

vertical height of δ [11,17], while the conventional scaling with the friction velocity $\omega^+ = \omega v/u_\tau^2$ is related to the near-wall region. Figure 7(a) shows V_T as a function of the threshold ω_{th}^* . The turbulent volume largely increases for $\omega_{th}^* < 10^{-4}$ as ω_{th}^* decreases because of very small values of vorticity magnitude in the nonturbulent region. The derivatives of V_T , $dV_T/d \log_{10}(\omega_{th}^*)$, are also calculated as a function of ω_{th}^* in Fig. 7(b). We can see that V_T hardly changes with ω_{th}^* for the range of $10^{-4} < \omega_{th}^* < 10^{-1}$, for which the location of the isosurface of vorticity magnitude hardly changes with ω_{th}^* . By comparing the curves for two groups in Fig. 7(a), V_T in group F is found to be flatter than group C in the range of $10^{-4} < \omega_{th}^* < 10^{-1}$, which indicates that the level of the numerical noise might be higher for group C.

The choice of the threshold is further discussed based on the joint probability density functions (JPDFs) of normalized vorticity magnitude ω^* and wall-normal distance y/δ [11], which are shown in Fig. 8 for the cases F002 and C002. Similar plots are obtained for F001 and C001 (not shown

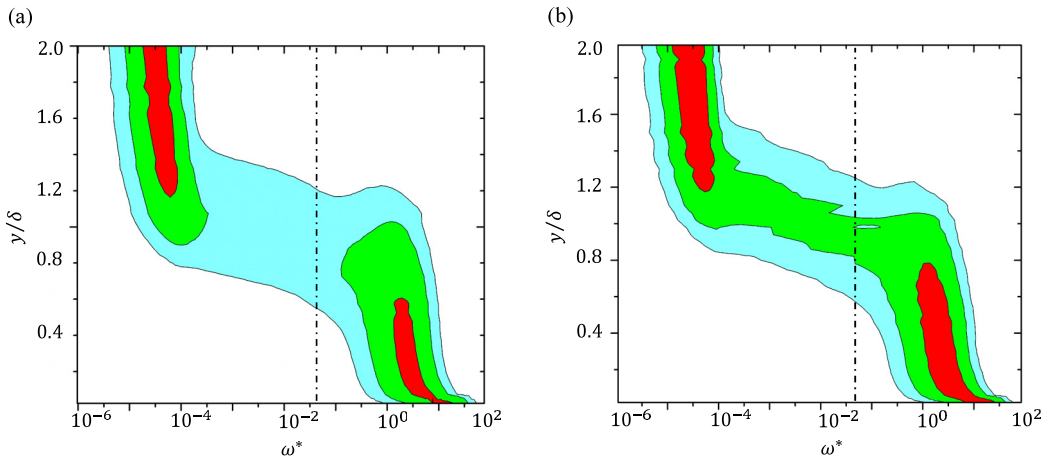


FIG. 8. JPDFs of normalized vorticity magnitude ω^* and vertical height y/δ . Contours contain 9%, 40%, and 50% of the fluid element, which are shown with cyan, green, and red, respectively, for (a) case F002 and (b) case C002.

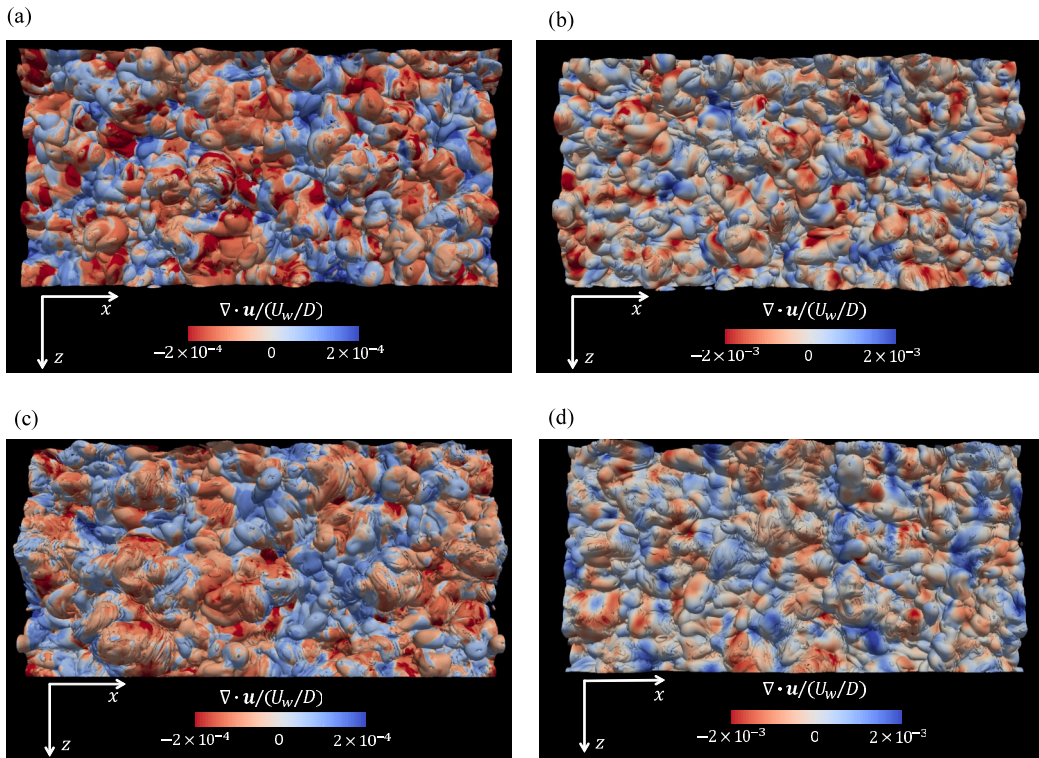


FIG. 9. Visualization of the irrotational boundary forming at the outer edge of the TNTI layer for (a) case F001, (b) case F002, (c) case C001, and (d) case C002. Color represents dilatation $\nabla \cdot \mathbf{u}$.

here). The JPDFs are also useful to examine the spatial distribution of vorticity. In the figure, the red, green, and cyan contours contain 50%, 40%, and 9% of the fluid element in the computational domain, respectively, where the residual 1% fluid element can be ignored. The turbulent core region corresponds to the bottom right corner (namely, low height and strong vorticity), while the small vorticity magnitude in the top left corner is the vorticity in the freestream, which could arise by pressure wave radiations and numerical error. In the case F002, we can see that the distribution of the JPDF significantly changes around $y/\delta = 1$ in Fig. 8(a), where most fluids appear in the bottom right corner with large vorticity magnitude or top left corner with very small vorticity magnitude and a low probability for finding a fluid with intermediate values of vorticity magnitude [the center of Fig. 8(a)]. This corresponds to a sharp jump in enstrophy found across the TNTI layer in previous studies [4]. In contrast, the JPDF for the case C002 shown in Fig. 8(b) exhibits a relatively large probability for a moderate level of vorticity magnitude around $y/\delta = 1$, although this region should consist of mostly turbulent fluid with large vorticity magnitude and nonturbulent fluid with small vorticity magnitude, while a very thin TNTI layer with moderate level of vorticity magnitude is expected to occupy only a small fraction of volume.

We use $\omega_{\text{th}}^* = 5.012 \times 10^{-2}$ [$\log_{10}(\omega_{\text{th}}^*) = -1.3$] indicated by the dashed lines shown in Fig. 8, to detect the turbulent region without including the region with small vorticity magnitude, where the irrotational boundary is represented as the isosurface of $\omega = \omega_{\text{th}}$. This threshold is on the plateau of V_T in Fig. 7(a), where the turbulent volume is not sensitive to the choice of the threshold.

The top views of the irrotational boundary from the whole DNS data set are visualized in Fig. 9, where the color shows dilatation $\nabla \cdot \mathbf{u} = -(D\rho/Dt)/\rho$. Positive and negative values of dilatation indicate the regions with fluid expansion and compression, respectively. We can see that both compression and expansion regions coexist on the irrotational boundary, where the dilatation at

TABLE II. Average resolution at the irrotational boundary.

Case	M	$\langle y_I \rangle / \delta$	$\langle \Delta x_I \rangle$	$\langle \Delta y_I \rangle$	$\langle \Delta z_I \rangle$
F001	0.8	0.85	$1.36\eta_c$	$1.42\eta_c$	$1.36\eta_c$
F002	1.6	0.83	$1.59\eta_c$	$1.36\eta_c$	$1.50\eta_c$
C001	0.8	0.87	$2.69\eta_c$	$1.80\eta_c$	$1.39\eta_c$
C002	1.6	0.87	$2.57\eta_c$	$1.84\eta_c$	$1.49\eta_c$

$M = 1.6$ (cases F002 and C002) is larger in magnitude than at $M = 0.8$ (cases F001 and C001) by a factor of $\sim 10^1$. The irrotational boundary exhibits structures with various length scales, which are the imprints of turbulent structures underneath the TNTI layer [18,56]. We have computed the average resolution on the irrotational boundary (Δx_I , Δy_I , Δz_I), which is obtained by taking the average of the mesh size at the grid points of all irrotational boundary locations. Table II shows Δx_I , Δy_I , and Δz_I in comparison with the Kolmogorov length scale in the turbulent core region η_c . Here we use the value at $y = 0.5\delta$ as the reference in the turbulent core region since nonturbulent fluids hardly reach this height. It should be stressed that although the TNTI appears in the intermittent region, the Kolmogorov scale η_c should be taken from the turbulent core region without including any contributions from nonturbulent fluids because the intermittent region contains both turbulent and nonturbulent fluids [21,57]. When η is computed in the intermittent region without excluding the contribution from the nonturbulent fluid, the value of η tends to be much larger than η_c since the nonturbulent flow has very large η [21,57]. In the present DNS, the average grid spacing at the outer edge of TNTI layer is about $1.5\eta_c$ in three directions in group F, which is close to the resolution in recent DNS of free shear flows used to study the TNTI [42,58]. However, group C, where the grid size is determined solely from the wall unit, does not have a resolution high enough to study the small scale near the TNTI especially in the x direction, where group C has the streamwise grid spacing determined based on the suggestion $\Delta x^+ < 9.7$ by Moser *et al.* [41]. This is almost double the grid spacing in the spanwise direction $\Delta x^+ \approx 2\Delta z^+$. This setting is reasonable for the near-wall region because the flow near the walls was found to be dominated by alternating high- and low-speed streaks, which is elongated in the streamwise direction [59]. However, the structure near the TNTI is very different from the near-wall region, resulting in the insufficient resolution near the TNTI in the streamwise direction for $\Delta x^+ \approx 2\Delta z^+$. It is also important to be careful with the grid size in the wall-normal direction near the TNTI layer since it is conventional to use finer grids near the wall and larger grid spacing in the intermittent region.

From comparisons between groups F and C in Fig. 9, we can clearly see how the resolution near the TNTI affects the geometry of the TNTI. It should be noted that the DNS of group C has a mesh size small enough to resolve the near-wall structure and provides global statistics, such as mean velocity and second-order statistics, similar to those for group F. However, the influence of insufficient resolution in group C is crucial in the visualization in Figs. 9(c) and 9(d): Many stripy patterns exist on the enstrophy isosurface, which is hardly seen in the DNS of incompressible free shear flows [42,57,58]. On the contrary, the enstrophy isosurface visualized in group F [Figs. 9(a) and 9(b)] is much smoother and is similar to those obtained in previous DNSs [42,57,58] and also of compressible shear layers [22]. It seems that the stripy patterns orthogonal to the streamwise direction in group C are caused by the insufficient resolution in the streamwise direction near the TNTI. The numerical noise, or oscillation in variables solved in the DNS, can produce the vorticity in the nonturbulent region near the TNTI. This explains different vorticity distributions between groups C and F in Fig. 8, which result in a difficulty in the detection of irrotational boundary in group C.

Figure 10 shows the near-wall vortical structures with the irrotational boundary for case F001, where the semitransparent surface on the upper left side is the irrotational boundary and the near-wall vortical structures are shown with blue-white color indicating the streamwise velocity u . The

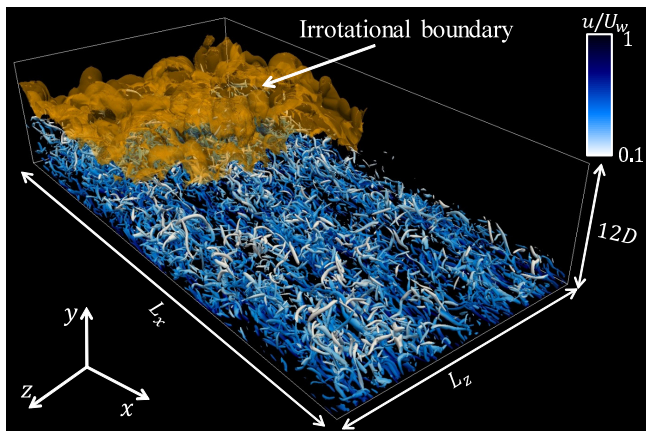


FIG. 10. Near-wall vortical structures visualized by the isosurface of $Q/(U_w/D) = 0.15$ colored by the streamwise velocity u and visualization of the irrotational boundary on the upper side for case F001.

vortical structures are visualized with the isosurface of the second invariant of velocity gradient tensor $Q/(U_w/D) = 0.15$, where $Q = [2(\nabla \cdot \mathbf{u})^2 + \omega_i \omega_i - 2S_{ij}S_{ij}]/4$. We can see the well-known hairpinlike structures near the wall, while the irrotational boundary appears above these structures. The average height of the irrotational boundary $\langle y_I \rangle$ is also shown in Table II, where the mean height is about 0.85 times the boundary layer thickness δ in all cases.

B. Dependence on threshold value for interface detection

For examining the robustness of the irrotational boundary location detected with vorticity magnitude, the isoline of vorticity magnitude is visualized for different thresholds in Fig. 11 for case F001. All of the threshold values are taken in the range of gray shadow shown in Fig. 7. We can see that the irrotational boundary does not change much for these thresholds. For the relatively small values (green and red lines), some bubbles of turbulent fluids appear surrounded by nonturbulent fluids. In contrast, small bubbles of nonturbulent fluids appear under the irrotational boundary when

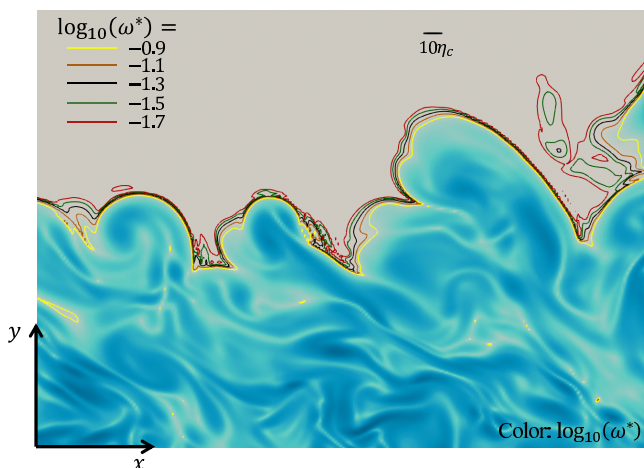


FIG. 11. Visualization of the irrotational boundary detected by different threshold values.

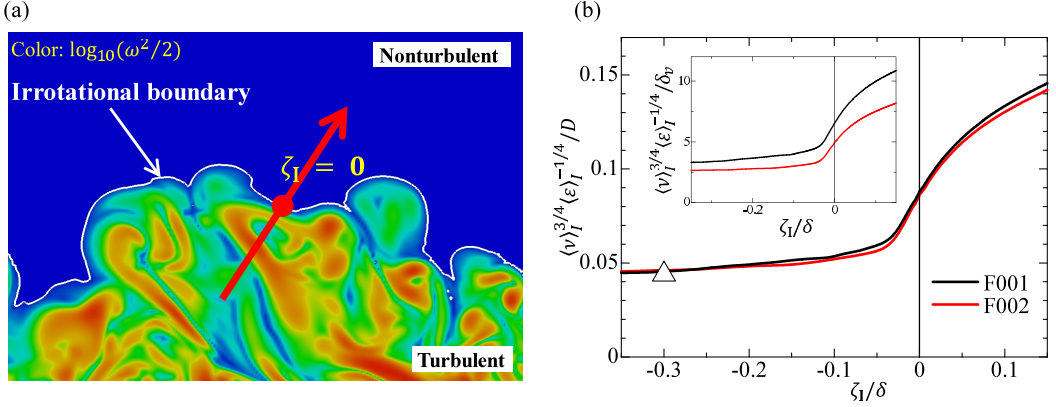


FIG. 12. (a) Definition of the local coordinate ζ_I used for computing conditional statistics on the distance from the irrotational boundary. (b) Conditional profiles of the Kolmogorov length scale defined with conditional average. Here \triangle shows the location where the Kolmogorov scale is used as the reference length scale of turbulence near the TNTI. The inset shows the Kolmogorov scale normalized by the viscous unit.

it is detected by a relatively large threshold (yellow line). The black and khaki lines detected by $\log_{10}(\omega^*) = -1.3$ and -1.1 are smoother and cause fewer bubbles, indicating that these are more appropriate thresholds than the other values in Fig. 11. Figure 11 also shows the size of $10\eta_C$. For $\log_{10}(\omega^*) = -1.3$ and -1.1 , the location of the irrotational boundary is different by several times η_C . Therefore, the range of $\log_{10}(\omega^*) = -1.3 \sim -1.1$ is a reasonable choice for a threshold value, and $\log_{10}(\omega^*) = -1.3$ is used in the present study.

C. Conditional statistics on the distance from the TNTI

Since the irrotational boundary detected as the enstrophy isosurface is located at the outer edge of the TNTI layer (an isosurface of vorticity magnitude $\sqrt{\omega_i \omega_i} = \omega_{th}$ is the same as an isosurface of enstrophy $\omega_i \omega_i / 2 = \omega_{th}^2 / 2$), the TNTI layer can be found just inside the irrotational boundary. The local coordinate ζ_I as shown in Fig. 12(a) is used to compute the statistics conditioned on the distance from the irrotational boundary. The location of the irrotational boundary is represented by $\zeta_I = 0$ as the origin of the local coordinate system. The direction of ζ_I is normal to the irrotational boundary, which is defined with the enstrophy gradient at the irrotational boundary

$$\mathbf{n} = -\nabla \omega^2 / |\nabla \omega^2|. \quad (20)$$

Positive/negative ζ_I points in the nonturbulent/turbulent region. Hereafter, the subscript I denotes the conditional statistic and the conditional average is denoted by $\langle \rangle_I$.

Figure 12(b) shows the conditional profiles of the Kolmogorov scale defined as $\langle v \rangle_I^{3/4} / \langle \epsilon \rangle_I^{1/4}$. The Kolmogorov scale is quite large in the nonturbulent region, decreases rapidly from the nonturbulent to the turbulent region, and then tends to be uniform in the turbulent core region. Similar profiles of Kolmogorov scale near the TNTI were also seen in Refs. [21,57]. The kinetic energy dissipation is non-negligible in the nonturbulent region because of the strain field due to large-scale motions [60,61]. The geometry and statistical properties of the TNTI layer are characterized by the properties of turbulence in the turbulent region below the TNTI layer [56,62]. In the present study, the Kolmogorov scale at the location $\zeta_I / \delta = -0.3$ shown by a large triangle in Fig. 12(b), denoted by η_I , is used as the reference length scale of turbulence near the TNTI, and the conditional statistics are presented against ζ_I / η_I . The other reference scales of turbulence near the TNTI, e.g., the Kolmogorov velocity scale v_{η_I} , are also calculated from the conditional statistics at this location. The Kolmogorov scale normalized by viscous unit is also shown in the top left corner of Fig. 12(b); we can see that η_I under the TNTI is around 3 times the viscous length scale.

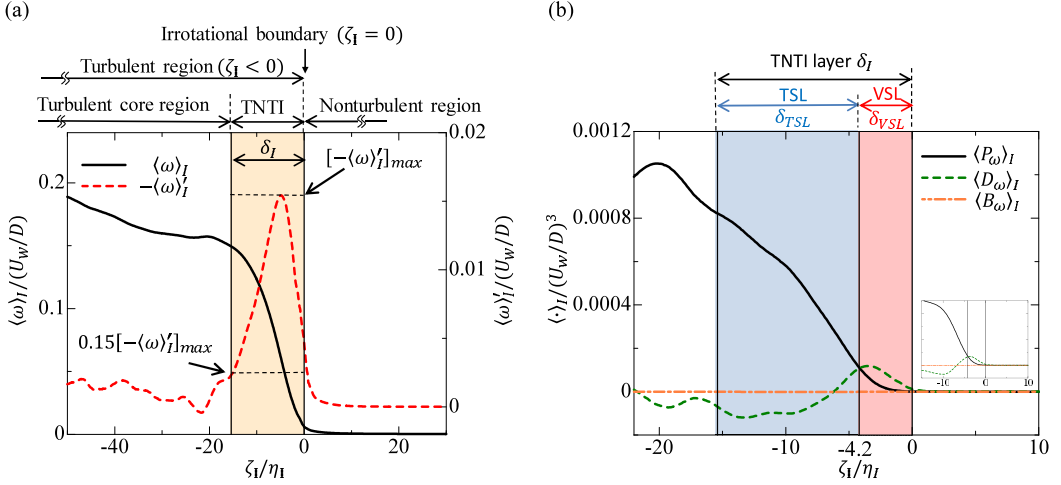


FIG. 13. (a) Conditional mean vorticity and its derivative with respect to ζ_I for case F001. (b) Conditional averages of enstrophy production P_ω , viscous diffusion D_ω , and baroclinic torque term B_ω for case F001. The inset shows the results for case F002. These figures also define the TNTI layer, VSL, TSL, and turbulent core region.

We investigate the structure of the TNTI layer, which is divided into the VSL and TSL. The TNTI layer can be defined as a region where the vorticity magnitude is adjusted between the turbulent and nonturbulent regions and is characterized by a large gradient in vorticity magnitude. Therefore, we can quantify the mean extent of the TNTI layer based on the derivative of $\langle \omega \rangle_I$ with respect to ζ_I following Ref. [63]. The examples of $\langle \omega \rangle_I$ and $-\langle \omega \rangle'_I = -d\langle \omega \rangle_I/d\zeta_I$ are shown in Fig. 13(a) for case F001 ($M = 0.8$). The mean thickness of the TNTI layer δ_I is defined based on the location where $-\langle \omega \rangle'_I$ reaches 15% of its maximum value as in Fig. 13(a). Therefore, the region of $-15.4 < \zeta_I/\eta_I < 0$ can be defined as the TNTI layer for F001.

The inner structures of the TNTI layer are well distinguished by vorticity dynamics, where the enstrophy evolves according to the transport equation [64,65]

$$\frac{D\omega^2/2}{Dt} = \omega_i S_{ij} \omega_j - \omega_i \omega_i \nabla \cdot \mathbf{u} + \frac{1}{\rho^2} \omega_i \varepsilon_{ijk} \frac{\partial P}{\partial x_j} \frac{\partial \rho}{\partial x_k} + \omega_i \varepsilon_{ijk} \frac{\partial}{\partial x_j} \left(\frac{1}{\rho} \frac{\partial \tau_{kl}}{\partial x_l} \right). \quad (21)$$

The terms on the right-hand side are the production term P_ω due to vortex stretching and compression, dilatation term Θ_ω , baroclinic torque term B_ω , and viscous term V_ω , respectively. The viscous term can further be divided into four terms: the viscous diffusion term D_ω , the viscous dissipation term ε_ω , the viscous torque term S_ω , and the term arising from the temperature dependence of viscosity μ_ω :

$$\begin{aligned} \omega_i \varepsilon_{ijk} \frac{\partial}{\partial x_j} \left(\frac{1}{\rho} \frac{\partial \tau_{kl}}{\partial x_l} \right) &= \nu \frac{\partial^2 \omega^2/2}{\partial x_j^2} - \nu \left(\frac{\partial \omega_i}{\partial x_j} \right)^2 - \frac{1}{\rho^2} \varepsilon_{ijk} \omega_i \frac{\partial \tau_{kn}}{\partial x_n} \frac{\partial \rho}{\partial x_j} \\ &\quad + \varepsilon_{ijk} \frac{1}{\rho} \omega_i \left(\frac{\partial \tau_{kn}/\mu}{\partial x_n} \frac{\partial \mu}{\partial x_j} + \frac{\tau_{kn}}{\mu} \frac{\partial \mu}{\partial x_n} \right). \end{aligned} \quad (22)$$

Previous DNS studies have used the ratio between the production and viscous diffusion terms for defining the VSL [64]. The conditional averages of P_ω , D_ω , and B_ω are shown in Fig. 13(b) for the both cases of F001 and F002. At the irrotational boundary ($\zeta_I = 0$), these terms are very small, which confirms that the isosurface with $\omega_{th}^* = 5.012 \times 10^{-2}$ is located at the outer edge of the TNTI layer. We can see that these two terms begin to deviate from 0 from the irrotational boundary ($\zeta_I = 0$) toward the turbulent region. The viscous diffusion term is larger than the production term near the

TABLE III. Mean thicknesses of the TNTI layer, VSL, and TSL normalized by the Kolmogorov scale and Taylor scale in the turbulent region near the TNTI layer.

Case	M	TNTI layer δ_I	δ_{VSL}	δ_{TSL}
F001	0.8	$15.4\eta_I/0.96\lambda_I$	$4.2\eta_I$	$11.2\eta_I$
F002	1.6	$16.3\eta_I/0.97\lambda_I$	$4.2\eta_I$	$12.1\eta_I$
C001	0.8	$18.7\eta_I/1.08\lambda_I$	$4.4\eta_I$	$14.3\eta_I$
C002	1.6	$20.4\eta_I/1.17\lambda_I$	$4.4\eta_I$	$16.0\eta_I$

irrotational boundary as found in many incompressible turbulent flows [64–66] and compressible shear layers [20]. The conditional average of the baroclinic torque term B_ω is almost zero near the TNTI layer. The results from F002 are shown in the inset of Fig. 13(b): The conditional average of these terms has a similar profile for both Mach numbers. Even though the baroclinic torque can generate enstrophy in the nonturbulent region, the conditional average of this term is close to zero near the TNTI layer in the present DNS. DNS of compressible mixing layers [22] showed that it becomes more important within the TNTI layer as the convective Mach number increases. However, the enstrophy in the nonturbulent region is still small enough to detect the turbulent fluid with enstrophy in their DNS [22]. The baroclinic torque might play an important role in the enstrophy generation in the nonturbulent region if the Mach number is much higher, such as in hypersonic flows.

The mean position of the VSL can be identified as the region with $\langle D_\omega \rangle_I > \langle P_\omega \rangle_I$ near the irrotational boundary following Refs. [20,54], where we can obtain the mean thickness of the VSL as $\delta_{\text{VSL}} = 4.2\eta_I$ from Fig. 13(b). Thus, the region of $-15.4 \leq \zeta_I/\eta_I \leq -4.2$ corresponds to the TSL, where the inviscid process (production term) has a larger contribution to the increase of the enstrophy. The TSL is also regarded as a buffer region between the VSL and the turbulent core regions [65]. The conditional statistics of the vorticity and enstrophy budget for case F002 ($M = 1.6$) are similar to the ones of F001 ($M = 0.8$), and the mean thicknesses of the TNTI layer δ_I , the VSL δ_{VSL} , and the TSL δ_{TSL} for different Mach number M are shown in Table III, where the thicknesses are normalized by the Kolmogorov scale η_I or Taylor microscale $\lambda_I = 10\langle v \rangle_I \langle k_t \rangle_I / \langle \varepsilon \rangle_I$ ($2\langle k_t \rangle_I = \sum_{i=1}^3 [\langle u_i^2 \rangle_I - \langle u_i \rangle_I^2]$) is the turbulent kinetic energy defined with conditional average) near the TNTI (at $\zeta_I = -0.38$). Although the thicknesses of the TNTI layer and TSL slightly change with Mach number, the mean thickness of the TNTI layer is about $15\eta_I$ – $16\eta_I$ ($0.96\lambda_I$), the VSL is about $4\eta_I$, and the TSL is about $11\eta_I$ – $12\eta_I$ for group F. These values normalized by the Kolmogorov scale in group F are close to previous studies of free shear flows [4,54,67] and shear free turbulence [67]. However, δ_I in F001 and F002 exhibits a closer match when it is normalized by Taylor microscale. The present DNS is not enough to investigate the scaling of the thickness because the Reynolds-number range is limited.

The study of the TNTI with the large eddy simulation indicates that an insufficient resolution in simulations causes a thicker TNTI layer [68]. Indeed, the TNTI layer thickness tends to be larger for group C, which does not have a resolution high enough to resolve the smallest scale in the turbulence near the TNTI. Hereafter, all the statistical analysis in the following is done for group F.

Figure 14 shows the conditional rms density fluctuation defined as $\langle \rho \rangle_{I,\text{rms}} = \sqrt{\langle \rho^2 \rangle_I - \langle \rho \rangle_I^2}$ divided by the density in freestream ρ_∞ . Even for $M = 1.6$, $\langle \rho \rangle_{I,\text{rms}}$ is about 2% of ρ_∞ near the TNTI layer, and the direct influences of compressibility are small near the TNTI layer, as also expected from small turbulent Mach numbers in the outer region (Fig. 6).

D. Analysis of the entrainment process

The velocity of the irrotational boundary (enstrophy isosurface) movement \mathbf{u}^I can be written as a sum of fluid velocity \mathbf{u} and the propagation velocity \mathbf{v}^P (enstrophy isosurface propagation), i.e., $\mathbf{u}^I = \mathbf{u} + \mathbf{v}^P$, where $\mathbf{v}^P = v_n \mathbf{n}$. By the propagation of the irrotational boundary to the nonturbulent region, nonturbulent fluids pass through the irrotational boundary to the turbulent region, which is

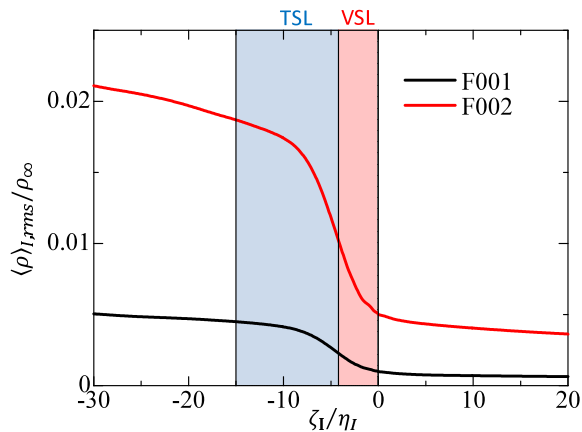
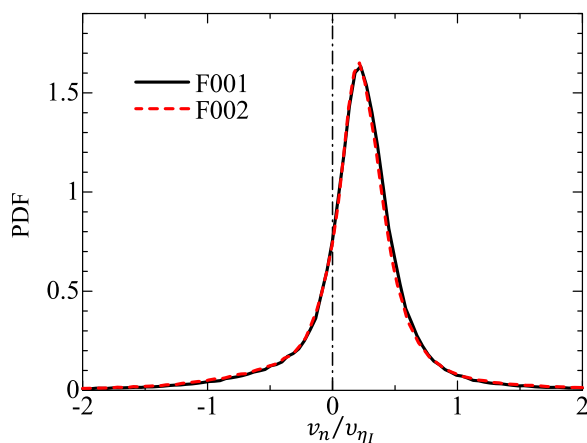


FIG. 14. Conditional rms density fluctuation.

also called the local entrainment [7]. The propagation velocity can be derived by considering a local coordinate which moves with the irrotational boundary [7]:

$$v_n = \frac{D(\omega^2/2)/Dt}{|\nabla(\omega^2/2)|} = \frac{P_\omega + \Theta_\omega + B_\omega + V_\omega}{|\nabla(\omega^2/2)|}. \quad (23)$$

The probability density functions (PDFs) of the propagation velocity v_n are shown in Fig. 15, where the propagation velocities are normalized by the Kolmogorov velocity $v_{\eta_I} = (\langle \varepsilon \rangle_I \langle \nu \rangle_I)^{1/4}$ in the turbulent core region near the TNTI at $\zeta_I = -0.3\delta$. The positive value of v_n indicates that the irrotational boundary propagates into the nonturbulent region. We can see that the irrotational boundary frequently propagates toward the nonturbulent region and hardly propagates toward the turbulent region, and the peak of propagation velocity is found to be of the order of the Kolmogorov velocity v_{η_I} . These results are similar to incompressible flows [7,54]. As described by the enstrophy transport equation, the terms on the right-hand side in Eq. (23) are the production term P_{v_n} , dilatation term Θ_{v_n} , baroclinic term B_{v_n} , and viscous term V_{v_n} , respectively. The conditional PDFs of these four terms are shown in Figs. 16(a) and 16(b), which reveal that the viscous term has the largest contribution of all terms, as found in previous studies [7,22,65,69]. As shown in Eq. (22), the


 FIG. 15. Conditional PDFs of the propagation velocity v_n .

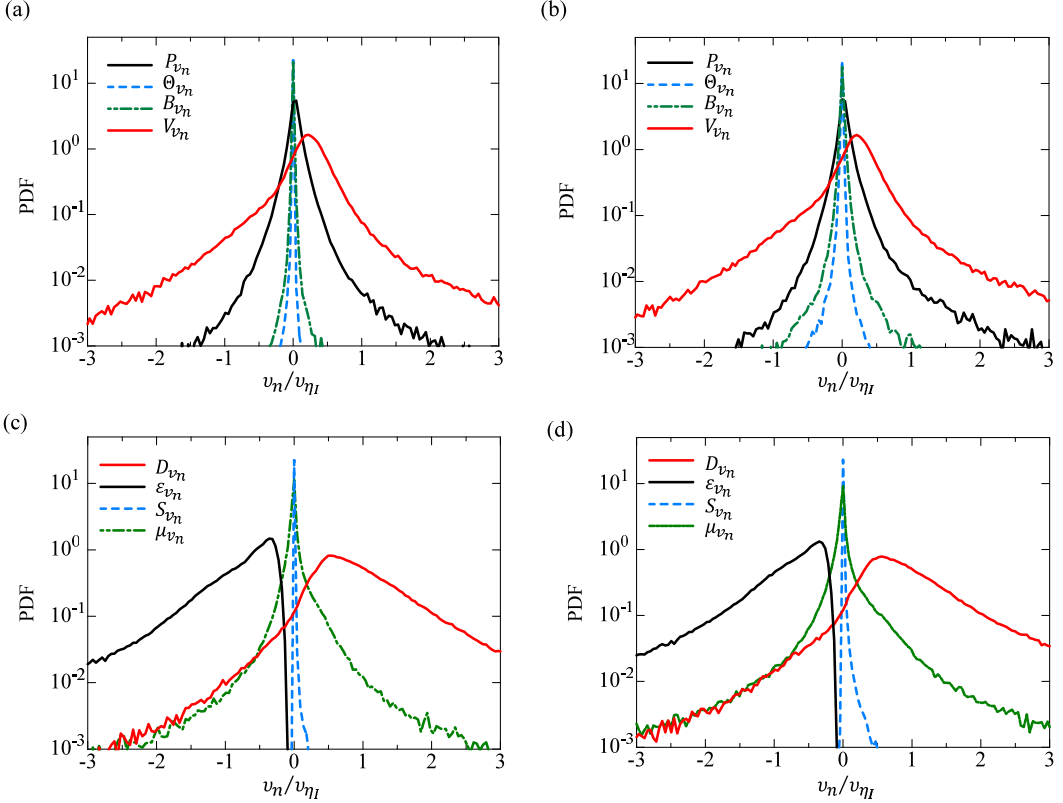


FIG. 16. Conditional PDFs of the propagation velocity decomposed into different terms as in Eq. (23) for (a) case F001 and (b) case F002 and conditional PDFs of contributions to V_{v_n} from different viscous effects presented in Eq. (22) for (c) case F001 and (d) case F002.

viscous effect on the propagation velocity can further be divided into four terms: the diffusion term D_{v_n} , the dissipation term ε_{v_n} , the viscous torque term S_{v_n} , and the term related to temperature dependence of viscosity μ_{v_n} , whose PDFs are shown in Figs. 16(c) and 16(d). We can see that a positive value of local entrainment is mainly contributed by the viscous diffusion, while the terms related to viscous torque and temperature dependence of viscosity are almost negligible. These results show that the local entrainment mechanism described as the enstrophy transport is hardly affected by compressibility for the Mach number considered here. This observation agrees with previous studies on compressible boundary layers, which have shown that compressibility effects are stronger in the near-wall region than in the outer region [48,53].

The entrainment is often explained by combination of the local transition from a nonturbulent to turbulent fluid near the TNTI and the nonturbulent fluid motion drawn toward the turbulent region, which are often called nibbling and engulfment, respectively [4]. To examine the nonturbulent fluid motion in the intermittent region, the conditional mean velocity in the wall-normal direction $\langle v \rangle_I$ is shown in Fig. 17; $\langle v \rangle_I$ has a distinct Z-shaped profile near the TNTI layer, which is consistent with the experimental results of the spatially developing boundary layer [15,70]. The average of v in the laboratory coordinate $\langle v \rangle$ is close to zero at any location in the temporal simulations of compressible boundary layers unlike in spatially developing boundary layers. However, the mean fluid motion in the wall-normal direction described by $\langle v \rangle_I$ is similar for both spatial and temporal boundary layers. We might observe differences in $\langle v \rangle_I$ between spatial and temporal boundary layers in the nonturbulent region very far from the TNTI (large ζ_I/δ that corresponds to the region of large y/δ , which is not included in the figure). In this region, $\langle v \rangle_I$ should be close to $\langle v \rangle$ because turbulent

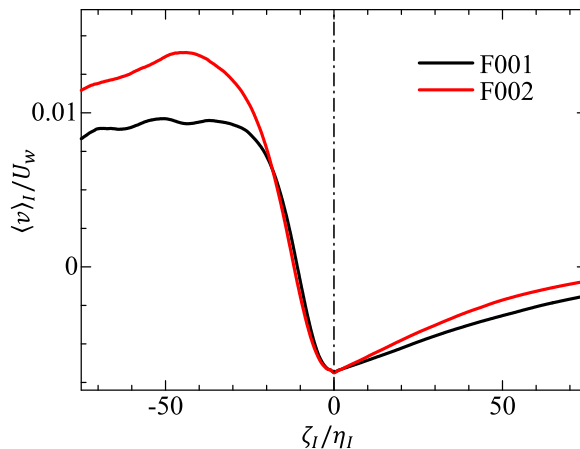


FIG. 17. Conditional profiles of the mean velocity in the wall-normal direction.

fluids do not reach this height. Negative $\langle v \rangle_I$ in the nonturbulent region is expected from the large-scale motion of TBLs, such as sweep motions and valley structures [39], which are expected to be related to the engulfment. Indeed, the nonturbulent fluid in the intermittent region was shown to have mean downward velocity in the spatially developing incompressible TBL [18], consistent with the present results for $\langle v \rangle_I$. Thus, the temporal simulation also captures well the process by which the nonturbulent fluids reach the TNTI, at least in the intermittent region.

To compare the mass entrainment between temporal and spatial TBLs, a feasible normalization method is required for the mass entrainment rate. In Ref. [27], both theoretical and DNS results confirmed that the momentum transport, which causes the growth of the boundary layer thickness δ , is dominated by the same term in both temporal and spatial incompressible TBLs at high Reynolds number ($C_f \lesssim 0.005$ in their simulations), where $U_w^+ d\delta/dX$ in temporal TBLs is close to $U_\infty^+ d\delta/dx$ in spatial TBLs ($X = tU_w$ is the temporal counterpart to x in spatial boundary layers). Furthermore, Chauhan *et al.* [13] showed that the averaged mass entrainment rate per unit horizontal area, denoted by f_m , can be calculated as $f_m = \rho_\infty U_\infty [d\delta/dx - d\delta^*/dx]$ in spatially developing incompressible TBLs, where δ^* is the displacement thickness and U_∞ is the freestream velocity. It is also shown that δ/δ^* is constant in both compressible and incompressible TBLs [1]. These studies indicate that the mass entrainment rate f_m normalized by $u_\tau \rho_\infty$ is useful for comparison between temporal and spatial TBLs. Hereafter, $f_{m,t}$ and $f_{m,s}$ represent f_m for temporal and spatial boundary layers, respectively.

First we examine $f_{m,s}/u_\tau \rho$ in experiments of spatially developing incompressible turbulent boundary layers at different Reynolds numbers [70] as shown in Table IV. The normalized mass flux is $f_{m,s}/u_\tau \rho \approx 0.33$ for both experiments, which is expected from the above discussion.

In terms of the TNTI, the mass entrainment rate is defined as the mass flux across the irrotational boundary. Then the mass entrainment rate per unit horizontal area in the temporal boundary layer is calculated as $f_{m,t} \approx \rho_\infty \langle v_n \rangle_I A_{IB}/L_x L_y$ from the present DNS, where $\langle v_n \rangle_I$ is taken at $\zeta_I = 0$ and A_{IB} is the surface area of irrotational boundary; the freestream density ρ_∞ used here is

TABLE IV. Normalized mean mass entrainment rate per unit horizontal area in previous experiments of incompressible TBLs for $Re_\tau = 7870$ and $14\,500$ [70].

Re_τ	7870	14 500
$f_{m,s}/u_\tau \rho$	0.333	0.333

TABLE V. Normalized mean mass entrainment rate per unit horizontal area in compressible TBLs. The temporal TBLs in the present DNS are compared with spatial compressible TBLs, where the entrainment rate is computed from the theoretical results of compressible TBLs [1].

M	$f_{m,t}/u_\tau \rho_\infty$	$f_{m,s}/u_\tau \rho_\infty$
0.8	0.355	0.347
1.6	0.398	0.392

because the compressibility is very weak near the irrotational boundary as shown in Fig. 14. On the other hand, the averaged mass entrainment rate in spatially developing compressible TBLs can be calculated by $f_{m,s} = \rho_\infty U_\infty [d\delta/dx - d\delta^*/dx]$ based on the compressible TBL theory [1]: The theory of boundary layer thickness in incompressible TBLs $\delta^{5/4} = 0.289(\mu_\infty/\rho_\infty U_\infty)^{1/4} x$ is also useful for compressible flow, because the boundary layer thickness δ does not depend significantly on the Mach number; the displacement thickness δ^* in compressible TBLs, defined as $\delta^* = \int_0^\infty (1 - \rho u/\rho_\infty U_w) dy$, can be calculated by the relation of $\delta^*/\delta = 1 - 7F(M)/2\beta$ for compressible TBLs [1], where $F(M) = \alpha_1^3 \ln[\alpha_1/(\alpha_1 - 1)] - \alpha_1^2 - \alpha_1/2 - 1/3$, $\alpha_1 = 1 + 1/\beta$, $\beta = r(\gamma - 1)M^2/2$, and $r \approx 0.9$ for zero-pressure-gradient boundary layer. The above equations with the parameters in the present DNSs give the averaged mass entrainment in spatially developing compressible TBLs. Table V shows $f_{m,t}/u_\tau \rho_\infty$ and $f_{m,s}/u_\tau \rho_\infty$ for $M = 0.8$ and 1.6. For both Mach numbers, $f_{m,t}/u_\tau \rho_\infty$ and $f_{m,s}/u_\tau \rho_\infty$ have similar values, confirming that the mass entrainment rate per unit horizontal area is similar in both spatial and temporal TBLs. It is also clear that $f_{m,t}/u_\tau \rho_\infty$ and $f_{m,s}/u_\tau \rho_\infty$ are larger for $M = 1.6$ than for $M = 0.8$. Values of $f_{m,t}/u_\tau \rho_\infty$ and $f_{m,s}/u_\tau \rho_\infty$ for $M = 0.8$ are very close to those obtained in incompressible experiments summarized in Table IV.

The propagation velocity (23) shows the speed at which the nonturbulent fluid crosses the outer edge of the TNTI layer. We consider the mass entrainment across the TNTI layer below, where we introduce a local coordinate system (\mathbf{x}^l, t') moving with the irrotational boundary. The origin of the local coordinate system is located on the irrotational boundary, while t' represents the time in this local coordinate. The original coordinate system (\mathbf{x}, t) , whose origin is located at the center of the computational domain, is referred to as a fixed coordinate system hereafter. The location of $\mathbf{x} = \mathbf{x}_0^l$ in the fixed coordinate system is assumed to be located on the irrotational boundary (the origin of the local coordinate system). By considering the coordinate transformation from the fixed coordinate system (\mathbf{x}, t) to the local coordinate system (\mathbf{x}^l, t') , the continuity equation in this local coordinate system can be derived as [71]

$$\frac{\partial \rho}{\partial t'} = -\nabla \cdot \{\rho[\mathbf{u}(\mathbf{x}_0^l + \mathbf{x}^l) - \mathbf{u}^l]\}, \quad (24)$$

where \mathbf{u}^l is the velocity of irrotational boundary movement. A similar equation for the passive scalar in incompressible flows was also used in previous studies [54, 72]. The term on the right-hand side in Eq. (24) represents the pseudotransport of mass due to the relative velocity $\Delta \mathbf{u}^l \equiv \mathbf{u}(\mathbf{x}_0^l + \mathbf{x}^l) - \mathbf{u}^l$ in the local coordinate system. The relative velocity can be written as

$$\Delta \mathbf{u}^l \equiv \mathbf{u}(\mathbf{x}_0^l + \mathbf{x}^l) - \mathbf{u}^l = \mathbf{u}(\mathbf{x}_0^l + \mathbf{x}^l) - \mathbf{u}(\mathbf{x}_0^l) - \mathbf{v}^P, \quad (25)$$

where $\mathbf{u}(\mathbf{x}_0^l + \mathbf{x}^l) - \mathbf{u}(\mathbf{x}_0^l)$ is the fluid velocity difference and \mathbf{v}^P is the propagation velocity. The fluid velocity difference is 0 at the irrotational boundary, which reveals that the mass transport is provided by the local entrainment at the irrotational boundary. The normalized mass flux $\mathbf{f} = \rho \Delta \mathbf{u}^l / \rho_\infty U_w$ in the local coordinate can be divided into two components: an irrotational boundary normal component $f_N = \mathbf{f} \cdot \mathbf{n} / \rho_\infty U_w$ and a tangential component $f_T = |\mathbf{f} - f_N \mathbf{n}|$. Because the tangential component is arbitrarily directed on the plane perpendicular to \mathbf{n} , the magnitude of the tangential flux is considered. It should be noted that the mass flux itself represents the mass transfer

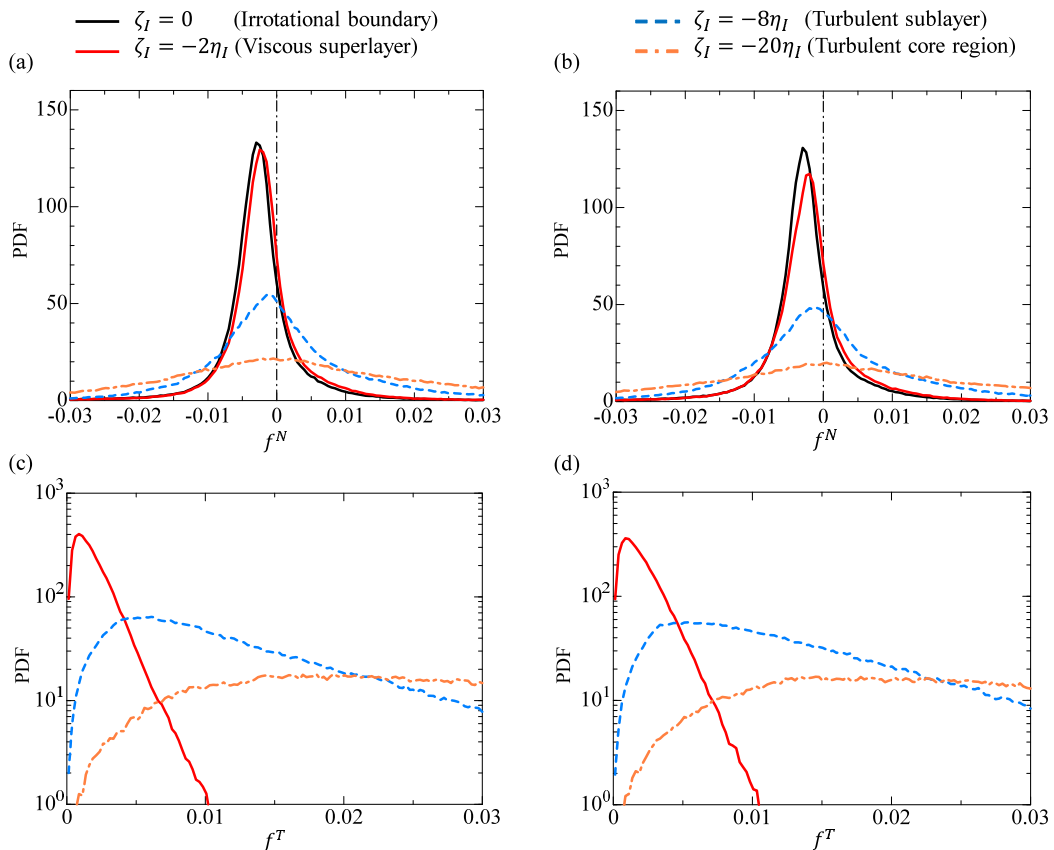


FIG. 18. Conditional PDFs of mass fluxes across the TNTI layer described by the relative velocity to the irrotational boundary near the TNTI. The mass fluxes are decomposed in (a) and (b) normal and (c) and (d) tangential components to the irrotational boundary for (a) and (c) case F001 and (b) and (d) case F002.

rather than the change in ρ at a given point, and a negative value of the normal component of mass flux f^N denotes the mass transfer toward the turbulent region.

Figure 18 shows the conditional PDFs of f^N and f^T , at several distances away from the irrotational boundary. The PDFs of the tangential component are not shown for the irrotational boundary because $f^T = 0$ at $\zeta_l = 0$. From these PDFs we can find that the mass fluxes for the normal component f^N are frequently negative at the irrotational boundary ($\zeta_l = 0$) and hardly depend on the location within the VSL, while the tangential component f^T has a very small value in the viscous superlayer. A large probability for negative f^N indicates a mass transfer from the nonturbulent toward the turbulent region in a large part of the VSL. In the TSL and turbulent core region, the PDFs are very different from the VSL: Both positive and negative values for f^N are observed and the tangential component f^T is no longer negligible compared with f^N .

To understand the relation between normal and tangential mass transfers, the conditional joint PDFs of f^N and f^T are shown in Fig. 19, where the JPDFs are taken from the VSL and TSL. We can find that the overall profile of the JPDF is very similar for both Mach numbers: $|f^N|$ is larger than f^T in most of the VSL [large probability for $|f^N| > f^T$ in Figs. 19(a) and 19(b)]; a large value of f^T can be found in the TSL. The dependence of the JPDF of the mass flux on the location within the VSL and TSL agrees well with the results obtained for a flux of passive scalar in incompressible flows [54]. These features can also be found in the conditional averages of f^N and f^T as shown in Table VI. The JPDF within the VSL confirms a continuous mass transfer in

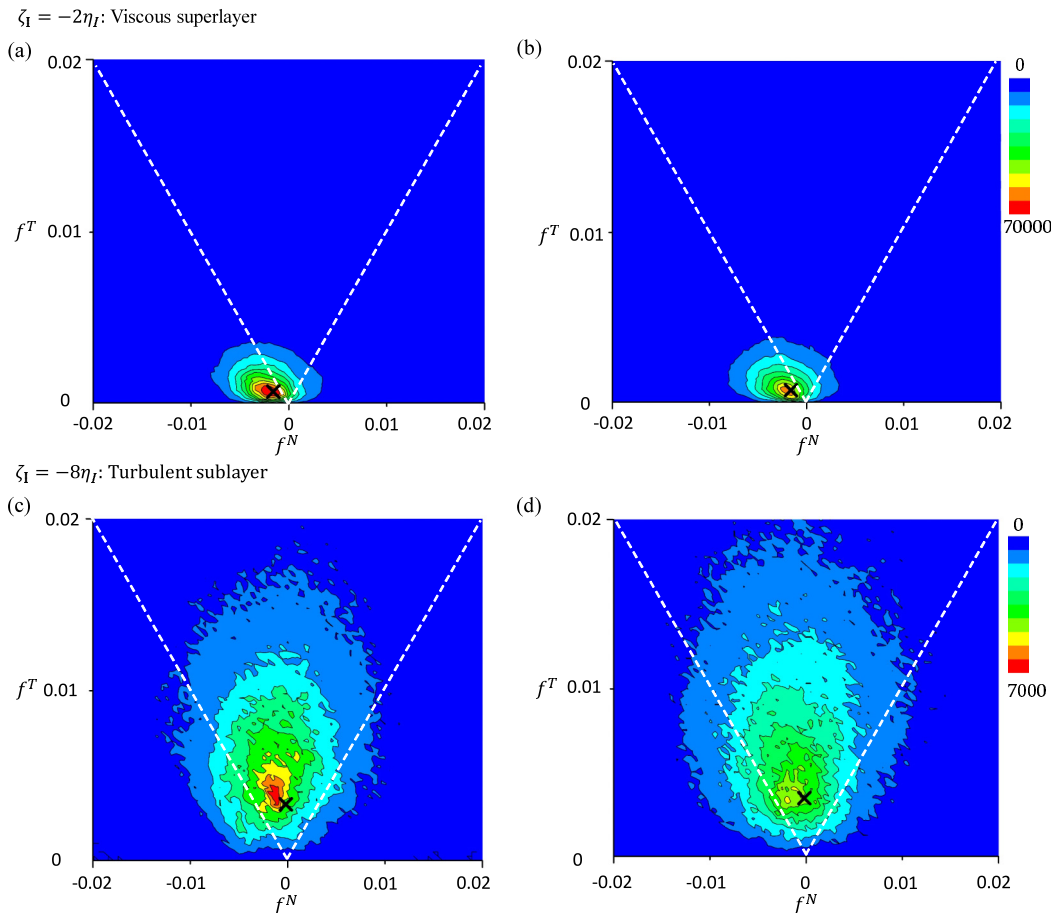


FIG. 19. Conditional JPDFs of the tangential and normal mass fluxes to the irrotational boundary within the VSL (at $\zeta_I = -2\eta_I$) and the TSL (at $\zeta_I = -8\eta_I$) for (a) and (c) case F001 and (b) and (d) case F002. The mass fluxes obtained by a single vortex model for the entrainment [62] at the same location of ζ_I are shown with crosses. White dashed lines denote $|f^N| = f^T$.

an irrotational boundary normal direction from the nonturbulent toward the TSL across the VSL, while the deentrainment, defined as the mass transfer from the turbulent to the nonturbulent region (positive f^N), hardly occurs. The TSL is characterized by a tangential mass transfer ($|f^N| < f^T$) for both Mach numbers. The tangential component f^T in the TSL can be larger than $|f^N|$ within the VSL. In the TSL, we can find both positive and negative values of f^N . The positive value of f^N within the TSL is related to the mass transfer from the turbulent core region toward the TSL. A large probability for both signs of f^N confirms that there exist fluids within the TSL coming from both the turbulent and nonturbulent regions. The existence of the fluid coming from the turbulent core region also explains more turbulentlike features of the TSL, such as strong inviscid effects in the enstrophy evolutions. The standard deviations defined with conditional average are also shown for f^N and f^T in Table VI. We can see that f^N has a larger fluctuation for case F002 within both the VSL and TSL, which implies that a larger magnitude of f^N appears for a higher Mach number.

The entrainment process described by f^N and f^T is compared with the entrainment model based on a single vortex proposed in Ref. [62]. It should be noted that we apply the model developed for incompressible flows because density fluctuations in the outer regions are very small even for

TABLE VI. Conditional averages $\langle \cdot \rangle_I$ and standard deviations $\sigma(\cdot)$ of the tangential and normal mass fluxes to the irrotational boundary within the VSL (at $\zeta_I = -2\eta_I$) and the TSL (at $\zeta_I = -8\eta_I$).

Case	M	$\langle f^N \rangle_I$	$\langle f^T \rangle_I$	$\sigma(f^N)$	$\sigma(f^T)$
VSL (at $\zeta_I = -2\eta_I$)					
F001	0.8	-0.58×10^{-2}	0.20×10^{-2}	0.47	0.15×10^{-2}
F002	1.6	-0.70×10^{-2}	0.22×10^{-2}	1.11	0.16×10^{-2}
TSL (at $\zeta_I = -8\eta_I$)					
F001	0.8	-0.25×10^{-2}	0.14×10^{-1}	0.34	0.11×10^{-1}
F002	1.6	-0.35×10^{-2}	0.15×10^{-1}	1.12	0.12×10^{-1}

$M = 1.6$. The model describes f^N and f^T on ζ_I as

$$f^N(\zeta_I) = -\frac{1}{2}\rho_\infty\alpha_2(L + \zeta_I), \quad (26)$$

$$f^T(\zeta_I) = \frac{\rho_\infty\Gamma_0}{2\pi} \left| \frac{1}{L + \zeta_I} \left[1 - \exp\left(-\frac{(L + \zeta_I)^2}{R_V^2}\right) \right] - \frac{1}{L} \left[1 - \exp\left(-\frac{L^2}{R_V^2}\right) \right] \right|, \quad (27)$$

with the model parameters of $L = \delta_{\text{VSL}} + R_V$, the constant radius of the vortex R_V , the strain rate for the steady Burgers vortex given by $\alpha_2 = 4\nu/R_V^2$, and the circulation Γ_0 , which defines the circulation Reynolds number $\text{Re}_\Gamma = \Gamma_0/\nu$. The relation of these quantities to the turbulence characteristics has been studied in the boundary layers [73], from which we take values of $R_V = 5\eta_I$ and $\text{Re}_\Gamma/\text{Re}_{\lambda_I}^{1/2} = 13.7$, where η_I , k_{tI} , and $\text{Re}_{\lambda_I} = \lambda_I(2k_{tI}/3)^{1/2}/\nu$ are taken in the turbulent region near the TNTI layer ($\zeta_I = -0.3\delta$). Here Re_{λ_I} is 70 for $M = 0.8$ and 72 for $M = 1.6$. The thickness of the VSL, δ_{VSL} , is taken from Table III. From the turbulence characteristics at $\zeta_I = -0.3\delta$, we can obtain $f^N(\zeta_I)$ and $f^T(\zeta_I)$ by Eqs. (26) and (27), which are shown with crosses in Fig 19. For both Mach numbers, the model estimates (f^N, f^T) fairly well, where (f^N, f^T) obtained by the model is located near the values with the largest probability in the plots. The mass transfer across the TNTI layer is well represented by the flow related to a single vortex, which describes the entrainment across the TNTI layer as a two-stage process: (i) The nonturbulent fluid is drawn toward the vortex core region within the VSL with the velocity related to the strain imposed on the vortex and (ii) the circular motion caused by the vortex transfers the fluid being entrained toward the turbulent core region.

V. CONCLUSION

We performed the DNS of subsonic and supersonic temporally evolving turbulent boundary layers to study the TNTI. We considered two different setups of the DNS, where in one case the grid spacing is determined solely based on the wall unit, while the other case uses a computational grid small enough to resolve the turbulent structures both underneath the TNTI and near the wall. We compared the global statistics between the present DNS and previous studies, showing that the DNSs with both grids reproduce well the first- and second-order statistics of the fully developed turbulent boundary layers. However, we have found that the spatial distribution of vorticity in the outer region is very sensitive to the spatial resolution near the TNTI. At the present Reynolds number $\text{Re}_\theta \approx 2200$, the DNS based on the grid size determined by the wall unit does not have sufficient resolution near the TNTI. The lack of resolution results in the spiky patterns of the enstrophy isosurface used to detect the outer edge of the TNTI layer and the thicker TNTI layer thickness. This problem can be solved by increasing the number of grid points, where a smoother enstrophy isosurface, similar to the previous studies of incompressible free shear flows, is obtained in the DNS with a grid small enough to resolve the Kolmogorov scale in the turbulent core region below the TNTI.

Based on the high-resolution DNS, we investigated the structure of the TNTI layer in compressible turbulent boundary layers. The present results show that the thickness of the TNTI layer, defined with a large gradient of conditional mean vorticity magnitude, is about 15 times the Kolmogorov scale η_l in turbulence near the TNTI layer. The inner (sub)layers of the TNTI layer are detected based on the vorticity dynamics, where the TSL and VSL are found to have thicknesses of $11\eta_l-12\eta_l$ and $4\eta_l$, respectively. These structures of the TNTI layer and their thicknesses divided by the Kolmogorov scale are very similar to those found in incompressible free shear flows. The compressibility effects at the Mach numbers $M = 0.8$ and 1.6 are very small within the TNTI layer, which appears in the outer intermittent region.

The local entrainment process was studied with the propagation velocity of the enstrophy isosurface, which represents the speed at which nonturbulent fluid crosses the outer edge of the TNTI layer. We showed that the compressibility effects are almost negligible for the propagation velocity, which is dominated by the viscous effects rather than a dilatational effect or baroclinic torque. The mean downward velocity is found in the nonturbulent region in the intermittent region, which is consistent with spatially evolving boundary layers [18,70]. The mass entrainment rate per unit horizontal area of the temporal TBLs is also consistent with the theoretical prediction [1] for the spatial compressible TBLs. This confirms that the dominant mechanism for the momentum transport, which is related to the TBL thickness growth, is not different between spatial and temporal compressible TBLs, as also found in incompressible TBLs [28]. Furthermore, the mass entrainment rate normalized by $u_\tau \rho_\infty$ at $M = 0.8$ also agrees well with experiments of spatially developing incompressible TBLs at various Reynolds numbers. The entrainment process across the TNTI layer was studied with the mass transport equation in the local coordinate system moving with the outer edge of the TNTI layer. The statistics of the mass flux show that the mass within the VSL is transferred toward the TSL in the direction normal to the TNTI, while the TSL is dominated by a tangential transfer. These mass fluxes within the VSL and TSL are compared with the single-vortex model for the entrainment within the TNTI layer, which was proposed for incompressible flows [62]. Because of very small effects of the compressibility in the outer region of the turbulent boundary layer, the entrainment model given by a single vortex predicts the mass flux within the TNTI layer fairly well, which strongly suggests the connection between the entrainment process within the TNTI layer and the small-scale vortical structures found underneath the TNTI layer of the turbulent boundary layers.

ACKNOWLEDGMENTS

The authors acknowledge Dr. A. Sekimoto for providing valuable comments. The numerical simulations presented in this paper were carried out on the high-performance computing system at Nagoya University and the high-performance computing system (NEC SX-ACE) at the Japan Agency for Marine-Earth Science and Technology. This work was partially supported by the Collaborative Research Project on Computer Science with High-Performance Computing in Nagoya University and by MEXT KAKENHI Grant No. 16K18013.

-
- [1] A. J. Smits and J. P. Dussauge, *Turbulent Shear Layers in Supersonic Flow* (Springer Science + Business Media, Berlin, 2006).
 - [2] L. Prandtl, Motion of fluids with very little viscosity, National Advisory Committee for Aeronautics Report No. 452, 1928 (unpublished).
 - [3] S. Corrsin and A. L. Kistler, Free-stream boundaries of turbulent flows, National Advisory Committee for Aeronautics Report No. TN-1244, 1955 (unpublished).
 - [4] C. B. da Silva, J. C. R. Hunt, I. Eames, and J. Westerweel, Interfacial layers between regions of different turbulence intensity, *Annu. Rev. Fluid Mech.* **46**, 567 (2014).

- [5] D. K. Bisset, J. C. R. Hunt, and M. M. Rogers, The turbulent/non-turbulent interface bounding a far wake, *J. Fluid Mech.* **451**, 383 (2002).
- [6] C. B. da Silva, R. J. N. Dos Reis, and J. C. F. Pereira, The intense vorticity structures near the turbulent/non-turbulent interface in a jet, *J. Fluid Mech.* **685**, 165 (2011).
- [7] M. Holzner and B. Lüthi, Laminar Superlayer at the Turbulence Boundary, *Phys. Rev. Lett.* **106**, 134503 (2011).
- [8] J. Mathew and A. J. Basu, Some characteristics of entrainment at a cylindrical turbulence boundary, *Phys. Fluids* **14**, 2065 (2002).
- [9] J. Westerweel, C. Fukushima, J. M. Pedersen, and J. C. R. Hunt, Mechanics of the Turbulent-Nonturbulent Interface of a Jet, *Phys. Rev. Lett.* **95**, 174501 (2005).
- [10] A. A. Townsend, *The Structure of Turbulent Shear Flow* (Cambridge University Press, Cambridge, 1976).
- [11] G. Borrell and J. Jiménez, Properties of the turbulent/non-turbulent interface in boundary layers, *J. Fluid Mech.* **801**, 554 (2016).
- [12] C. M. de Silva, J. Philip, K. Chauhan, C. Meneveau, and I. Marusic, Multiscale Geometry and Scaling of the Turbulent-Nonturbulent Interface in High Reynolds Number Boundary Layers, *Phys. Rev. Lett.* **111**, 044501 (2013).
- [13] K. Chauhan, J. Philip, C. M. de Silva, N. Hutchins, and I. Marusic, The turbulent/non-turbulent interface and entrainment in a boundary layer, *J. Fluid Mech.* **742**, 119 (2014).
- [14] J. Philip, C. Meneveau, C. M. de Silva, and I. Marusic, Multiscale analysis of fluxes at the turbulent/non-turbulent interface in high Reynolds number boundary layers, *Phys. Fluids* **26**, 015105 (2014).
- [15] C. M. de Silva, J. Philip, N. Hutchins, and I. Marusic, Interfaces of uniform momentum zones in turbulent boundary layers, *J. Fluid Mech.* **820**, 451 (2017).
- [16] T. Ishihara, H. Ogasawara, and J. C. R. Hunt, Analysis of conditional statistics obtained near the turbulent/non-turbulent interface of turbulent boundary layers, *J. Fluids Struct.* **53**, 50 (2015).
- [17] C. B. da Silva, R. R. Taveira, and G. Borrell, Characteristics of the turbulent/nonturbulent interface in boundary layers, jets and shear-free turbulence, *J. Phys.: Conf. Ser.* **506**, 012015 (2014).
- [18] J. Lee, H. J. Sung, and T. A. Zaki, Signature of large-scale motions on turbulent/non-turbulent interface in boundary layers, *J. Fluid Mech.* **819**, 165 (2017).
- [19] C. B. da Silva, The behavior of subgrid-scale models near the turbulent/nonturbulent interface in jets, *Phys. Fluids* **21**, 081702 (2009).
- [20] R. Jahanbakhshi, N. S. Vaghefi, and C. K. Madnia, Baroclinic vorticity generation near the turbulent/non-turbulent interface in a compressible shear layer, *Phys. Fluids* **27**, 105105 (2015).
- [21] N. S. Vaghefi and C. K. Madnia, Local flow topology and velocity gradient invariants in compressible turbulent mixing layer, *J. Fluid Mech.* **774**, 67 (2015).
- [22] R. Jahanbakhshi and C. K. Madnia, Entrainment in a compressible turbulent shear layer, *J. Fluid Mech.* **797**, 564 (2016).
- [23] J. Mathew, S. Ghosh, and R. Friedrich, Changes to invariants of the velocity gradient tensor at the turbulent-nonturbulent interface of compressible mixing layers, *Int. J. Heat Fluid Flow* **59**, 125 (2016).
- [24] S. E. Guarini, R. D. Moser, K. Shariff, and A. Wray, Direct numerical simulation of a supersonic turbulent boundary layer at Mach 2.5, *J. Fluid Mech.* **414**, 1 (2000).
- [25] M. P. Martín, Direct numerical simulation of hypersonic turbulent boundary layers. Part 1. Initialization and comparison with experiments, *J. Fluid Mech.* **570**, 347 (2007).
- [26] Z. Wang, J. Zhou, J. Fan, and K. Cen, Direct numerical simulation of ozone injection technology for NO_x control in flue gas, *Energy Fuels* **20**, 2432 (2006).
- [27] M. Kozul, D. Chung, and J. P. Monty, Direct numerical simulation of the incompressible temporally developing turbulent boundary layer, *J. Fluid Mech.* **796**, 437 (2016).
- [28] M. Kozul and D. Chung, Direct numerical simulation of the incompressible temporally developing turbulent boundary layer, in *Proceedings of the 19th Australasian Fluid Mechanics Conference*, edited by H. Chowdhury and F. Alam (Australasian Fluid Mechanics Society, 2014).
- [29] J. H. Lee, Y. S. Kwon, J. P. Monty, and N. Hutchins, Time-resolved PIV measurement of a developing zero pressure gradient turbulent boundary layer, in *Proceedings of the 19th Australasian Fluid Mechanics Conference*, edited by P. A. Brandner and B. W. Pearce (Australasian Fluid Mechanics Society, 2014).

- [30] A. Kempf, M. Klein, and J. Janicka, Efficient generation of initial- and inflow-conditions for transient turbulent flows in arbitrary geometries, *Flow Turbul. Combust.* **74**, 67 (2005).
- [31] G. Lodato, P. Domingo, and L. Vervisch, Three-dimensional boundary conditions for direct and large-eddy simulation of compressible viscous flows, *J. Comput. Phys.* **227**, 5105 (2008).
- [32] C. Bogey and C. Bailly, Turbulence and energy budget in a self-preserving round jet: Direct evaluation using large eddy simulation, *J. Fluid Mech.* **627**, 129 (2009).
- [33] Z. Wang, Y. Lv, P. He, J. Zhou, and K. Cen, Fully explicit implementation of direct numerical simulation for a transient near-field methane/air diffusion jet flame, *Comput. Fluids* **39**, 1381 (2010).
- [34] C. A. Kennedy and A. Gruber, Reduced aliasing formulations of the convective terms within the Navier-Stokes equations for a compressible fluid, *J. Comput. Phys.* **227**, 1676 (2008).
- [35] T. A. Zang, On the rotation and skew-symmetric forms for incompressible flow simulations, *Appl. Numer. Math.* **7**, 27 (1991).
- [36] M. H. Carpenter and C. A. Kennedy, Fourth-order 2N-storage Runge-Kutta schemes, NASA Report No. NASA-TM-109112, 1994 (unpublished).
- [37] C. A. Kennedy and M. H. Carpenter, Several new numerical methods for compressible shear-layer simulations, *Appl. Numer. Math.* **14**, 397 (1994).
- [38] Z. Wang, P. He, Y. Lv, J. Zhou, J. Fan, and K. Cen, Direct numerical simulation of subsonic round turbulent jet, *Flow Turbul. Combust.* **84**, 669 (2010).
- [39] S. B. Pope, *Turbulent Flows* (Cambridge University Press, Cambridge, 2000).
- [40] P. Schlatter and R. Örlü, Turbulent boundary layers at moderate Reynolds numbers: Inflow length and tripping effects, *J. Fluid Mech.* **710**, 5 (2012).
- [41] R. D. Moser, J. Kim, and N. N. Mansour, Direct numerical simulation of turbulent channel flow up to $Re_\tau = 590$, *Phys. Fluids*. **11**, 943 (1999).
- [42] M. Gampert, J. Boschung, F. Hennig, M. Gauding, and N. Peters, The vorticity versus the scalar criterion for the detection of the turbulent/non-turbulent interface, *J. Fluid Mech.* **750**, 578 (2014).
- [43] E. J. Hopkins and M. Inouye, An evaluation of theories for predicting turbulent skin friction and heat transfer on flat plates at supersonic and hypersonic Mach numbers, *AIAA J.* **9**, 993 (1971).
- [44] A. J. Smits, N. Matheson, and P. N. Joubert, Low-Reynolds-number turbulent boundary layers in zero and favorable pressure gradients, *J. Ship Res.* **27**, 147 (1983).
- [45] E. R. Van Driest, Turbulent boundary layer in compressible fluids, *J. Aeronaut. Sci.* **18**, 145 (1951).
- [46] M. Lagha, J. Kim, J. D. Eldredge, and X. Zhong, A numerical study of compressible turbulent boundary layers, *Phys. Fluids* **23**, 015106 (2011).
- [47] S. Pirozzoli, M. Bernardini, and F. Grasso, Characterization of coherent vortical structures in a supersonic turbulent boundary layer, *J. Fluid Mech.* **613**, 205 (2008).
- [48] T. Maeder, N. A. Adams, and L. Kleiser, Direct simulation of turbulent supersonic boundary layers by an extended temporal approach, *J. Fluid Mech.* **429**, 187 (2001).
- [49] C. Wenzel, B. Selent, M. Kloker, and U. Rist, DNS of compressible turbulent boundary layers and assessment of data/scaling-law quality, *J. Fluid Mech.* **842**, 428 (2018).
- [50] L. P. Erm and N. J. Peter, Low-Reynolds-number turbulent boundary layers, *J. Fluid Mech.* **230**, 1 (1991).
- [51] M. P. Simens, J. Jiménez, S. Hoyas, and Y. Mizuno, A high-resolution code for turbulent boundary layers, *J. Comput. Phys.* **228**, 4218 (2009).
- [52] M. V. Morkovin, Effects of compressibility on turbulent flows, *Mec. Turbul.* **367**, 380 (1962).
- [53] S. Pirozzoli and M. Bernardini, Turbulence in supersonic boundary layers at moderate Reynolds number, *J. Fluid Mech.* **688**, 120 (2011).
- [54] T. Watanabe, Y. Sakai, K. Nagata, Y. Ito, and T. Hayase, Turbulent mixing of passive scalar near turbulent and non-turbulent interface in mixing layers, *Phys. Fluids* **27**, 085109 (2015).
- [55] R. R. Prasad and K. R. Sreenivasan, Scalar interfaces in digital images of turbulent flows, *Exp. Fluids* **7**, 259 (1989).
- [56] C. B. da Silva and R. R. Taveira, The thickness of the turbulent/nonturbulent interface is equal to the radius of the large vorticity structures near the edge of the shear layer, *Phys. Fluids* **22**, 121702 (2010).
- [57] R. R. Taveira and C. B. da Silva, Kinetic energy budgets near the turbulent/nonturbulent interface in jets, *Phys. Fluids* **25**, 015114 (2013).

- [58] T. Watanabe, J. J. Riley, and K. Nagata, Effects of stable stratification on turbulent/nonturbulent interfaces in turbulent mixing layers, *Phys. Rev. Fluids* **1**, 044301 (2016).
- [59] R. D. Moser and P. Moin, Direct numerical simulation of curved turbulent channel flow, NASA Report No. TM-85974, 1984 (unpublished).
- [60] C. B. da Silva and J. C. F. Pereira, Invariants of the velocity-gradient, rate-of-strain, and rate-of-rotation tensors across the turbulent/nonturbulent interface in jets, *Phys. Fluids* **20**, 055101 (2008).
- [61] A. Attili, J. C. Cristancho, and F. Bisetti, Statistics of the turbulent/non-turbulent interface in a spatially developing mixing layer, *J. Turbul.* **15**, 555 (2014).
- [62] T. Watanabe, R. Jaulino, R. R. Taveira, C. B. da Silva, K. Nagata, and Y. Sakai, Role of an isolated eddy near the turbulent/non-turbulent interface layer, *Phys. Rev. Fluids* **2**, 094607 (2017).
- [63] T. Watanabe, J. J. Riley, and K. Nagata, Turbulent entrainment across turbulent-nonturbulent interfaces in stably stratified mixing layers, *Phys. Rev. Fluids* **2**, 104803 (2017).
- [64] R. R. Taveira and C. B. da Silva, Characteristics of the viscous superlayer in shear free turbulence and in planar turbulent jets, *Phys. Fluids* **26**, 021702 (2014).
- [65] M. van Reeuwijk and M. Holzner, The turbulence boundary of a temporal jet, *J. Fluid Mech.* **739**, 254 (2014).
- [66] M. Holzner, A. Liberzon, N. Nikitin, B. Lüthi, W. Kinzelbach, and A. Tsinober, A Lagrangian investigation of the small-scale features of turbulent entrainment through particle tracking and direct numerical simulation, *J. Fluid Mech.* **598**, 465 (2008).
- [67] T. S. Silva, M. Zecchetto, and C. B. da Silva, The scaling of the turbulent/non-turbulent interface at high Reynolds numbers, *J. Fluid Mech.* **843**, 156 (2018).
- [68] T. Watanabe, Y. Sakai, K. Nagata, and Y. Ito, Large eddy simulation study of turbulent kinetic energy and scalar variance budgets and turbulent/non-turbulent interface in planar jets, *Fluid Dyn. Res.* **48**, 021407 (2016).
- [69] T. Watanabe, C. B. da Silva, Y. Sakai, K. Nagata, and T. Hayase, Lagrangian properties of the entrainment across turbulent/non-turbulent interface layers, *Phys. Fluids* **28**, 031701 (2016).
- [70] K. Chauhan, J. Philip, and I. Marusic, Scaling of the turbulent/non-turbulent interface in boundary layers, *J. Fluid Mech.* **751**, 298 (2014).
- [71] T. Watanabe, Y. Sakai, K. Nagata, Y. Ito, and T. Hayase, Enstrophy and passive scalar transport near the turbulent/non-turbulent interface in a turbulent planar jet flow, *Phys. Fluids* **26**, 105103 (2014).
- [72] T. S. Silva and C. B. da Silva, The behavior of the scalar gradient across the turbulent/non-turbulent interface in jets, *Phys. Fluids* **29**, 085106 (2017).
- [73] H. Mouri, A. Hori, and Y. Kawashima, Laboratory experiments for intense vortical structures in turbulence velocity fields, *Phys. Fluids* **19**, 055101 (2007).